Pauls et al. Genome Medicine (2021) 13:168
https://doi.org/10.1186/s13073-021-00983-y

Genome Medicine

RESEARCH Open Access

Identification and drug-induced reversion of molecular signatures of Alzheimer's disease onset and progression in App^{NL-G-F}, App^{NL-F}, and 3xTg-AD mouse models

Eduardo Pauls[1†], Sergi Bayod[1†], Lídia Mateo[1†], Víctor Alcalde[1], Teresa Juan-Blanco[1], Marta Sánchez-Soto[1], Takaomi C. Saido[2], Takashi Saito[3], Antoni Berrenguer-Llergo[4], Camille Stephan-Otto Attolini[4], Marina Gay[5], Eliandre de Oliveira[6], Miquel Duran-Frigola[1] and Patrick Aloy[1,7*]

Abstract

Background: In spite of many years of research, our understanding of the molecular bases of Alzheimer's disease (AD) is still incomplete, and the medical treatments available mainly target the disease symptoms and are hardly effective. Indeed, the modulation of a single target (e.g., β-secretase) has proven to be insufficient to significantly alter the physiopathology of the disease, and we should therefore move from gene-centric to systemic therapeutic strategies, where AD-related changes are modulated globally.

Methods: Here we present the complete characterization of three murine models of AD at different stages of the disease (i.e., onset, progression and advanced). We combined the cognitive assessment of these mice with histological analyses and full transcriptional and protein quantification profiling of the hippocampus. Additionally, we derived specific Aβ-related molecular AD signatures and looked for drugs able to globally revert them.

Results: We found that AD models show accelerated aging and that factors specifically associated with Aβ pathology are involved. We discovered a few proteins whose abundance increases with AD progression, while the corresponding transcript levels remain stable, and showed that at least two of them (i.e., Ifit3 and Syt11) co-localize with Aβ plaques in the brain. Finally, we found two NSAIDs (dexketoprofen and etodolac) and two anti-hypertensives (penbutolol and bendroflumethiazide) that overturn the cognitive impairment in AD mice while reducing Aβ plaques in the hippocampus and partially restoring the physiological levels of AD signature genes to wild-type levels.

* Correspondence: patrick.aloy@irbbarcelona.org
†Eduardo Pauls, Sergi Bayod and Lídia Mateo contributed equally to this work.
[1]Joint IRB-BSC-CRG Programme in Computational Biology, Institute for Research in Biomedicine (IRB Barcelona), The Barcelona Institute of Science and Technology, Barcelona, Catalonia, Spain
[7]Institució Catalana de Recerca i Estudis Avançats (ICREA), Barcelona, Catalonia, Spain
Full list of author information is available at the end of the article

Conclusions: The characterization of three AD mouse models at different disease stages provides an unprecedented view of AD pathology and how this differs from physiological aging. Moreover, our computational strategy to chemically revert AD signatures has shown that NSAID and anti-hypertensive drugs may still have an opportunity as anti-AD agents, challenging previous reports.

Keywords: Alzheimer's disease, Transcriptomics, Proteomics, Data-driven drug discovery, In vivo models

Background

Alzheimer's disease (AD) is the most common form of dementia. The accumulation of amyloid-beta (Aβ) peptide in the form of plaques and the formation of intracellular Tau neurofibrillary tangles in the brain are the main pathological hallmarks of this neurodegenerative disease [1]. Mutations in genes that are part of the Aβ processing pathway (e.g., *APP*, *PSEN1,* and *PSEN2*) cause infrequent cases of hereditary AD [2]. This observation thus reinforces the hypothesis that Aβ accumulation plays a necessary role in AD onset. At a later stage, Aβ aggregation induces a series of molecular changes that lead to Tau hyper-phosphorylation and intracellular fibrillation, which in turn causes neuronal death and neurodegeneration [3].

Transgenic mice that develop extensive Aβ plaque aggregation have provided important insights into the pathobiology of AD and there is consensus that they are representative models of the asymptomatic stage of AD [4], although it is accepted that they are incomplete models of the disease. Mice expressing mutant forms of human *APP* recapitulate many aspects of cerebral Aβ accumulation seen in the human disease, including associated neuroinflammation, synaptic dysfunction, and vascular pathology [5]. Characterization of the molecular events taking place during Aβ aggregate accumulation in the brain is key to identifying signaling pathways that might be altered during AD and to unveiling potential biomarkers and therapeutic opportunities. Previous efforts to characterize murine models of AD at the transcriptional level have highlighted the role of inflammatory pathways in AD pathogenesis [6, 7]. Recently, key studies have addressed the role of neuroinflammation using single-cell sequencing strategies to identify specific microglial sub-populations associated with AD [8, 9]. Given the accumulation of proteins in the plaques, quantitative proteomics might also be a fundamental approach to understand protein-related changes in AD pathogenesis. Unfortunately, to date, these studies have been limited to single time points and decoupled from gene-expression data [10–14]. However, it is clear that combining transcriptional and proteomics data provides key insights into aging processes in rats [15].

Despite many advances in the characterization of different physiological motifs involved in AD onset and progression, our understanding of the events that trigger the disease is limited. Consequently, the only medical treatments currently available for AD are purely symptomatic and hardly effective [16], and most developments aiming at modifying the biology of the disease have failed [17]. The recurrent failures have triggered a debate about the deficiencies in diagnostic strategies, the choice of therapeutic targets, and the design of the clinical trials [18]. On the one hand, it seems clear that modulation of a single target, even with a highly efficient drug, is unlikely to yield the desired outcome, and there is a growing perception that we should increase the level of complexity of our proposed therapies from a gene-centric to a systems view [17]. Another aspect that has become apparent is that we have been studying AD and attempting to develop therapeutics against it at advanced stages of the disease when it is virtually impossible to reverse the brain damage already caused [19, 20]. We therefore need to focus on much earlier phases, ideally even before the first clinical symptoms appear or when cognitive impairment is still mild [18].

Unbiased genome-wide data-driven approaches may reveal new therapeutic opportunities, providing a global perspective beyond individual targets. For example, gene-expression data arising from a pathological phenotype can be seen as a disease-specific *signature* and used to find compounds able to restore a healthy state [21]. Indeed, this approach has been successfully used to identify drugs targeting obesity [22], osteoporosis [23], and aging [24] at preclinical stages. Recently, we extended the idea of using small molecules to mimic or revert biological signatures beyond transcriptional profiles and demonstrated the capacity of our approach to identify compounds able to revert specific expression alterations of AD genes (e.g., BIN1, GRIND2D) in APP^{V717F} and $PSEN1^{M146V}$ SH-SY5Y cells [25]. However, despite its potential, this approach to revert global signatures has been validated only in cell cultures and thus its in vivo relevance is still uncertain.

Here we present a comprehensive characterization of three murine AD models at phenotypic and molecular levels, including transcriptomic and proteomic profiles. We explore the molecular changes associated with AD onset, progression, and advanced stages, and correlate them with cognitive status and Aβ accumulation in order to study the dynamics of the disease and compare

the changes observed with healthy aging processes. Moreover, to pinpoint potential instances of protein aggregation, we examine those cases in which transcript levels and protein abundance are decoupled. Finally, we use the derived molecular profiles to identify approved drugs able to revert the specific AD signatures and we study their effects at phenotypic and molecular levels in vitro and in vivo (summarized in Fig. 1a).

Methods

Cells

SH-SY5Y cells (obtained from Jens Lüders' lab, IRB Barcelona) were cultured in DMEM/F12 (1:1) medium supplemented with 10% FBS, glutamine, and antibiotics (Thermo Fisher Scientific). 7PA2 cells overexpressing mutated APP were obtained from Dennis Selkoe's lab (Harvard Medical School, Boston). 7PA2 cells were maintained in DMEM medium supplemented with 10% FBS, glutamine, and antibiotics. CRISPR/Cas9-edited $PSEN1^{M146V/M146V}$ cells have been described before [25]. For RNA interference, we used pLKO.1-puro Mission shRNA vectors (Sigma-Aldrich). Target sequences are provided in Additional File 1: Table S7. Viral vectors were generated in 293T cells to infect SH-SY5Y cells that were selected with 2 μg/ml puromycin (Sigma-Aldrich), following the manufacturer's recommendations. For the assays on SH-SY5Y cells, 5×10^4 cells were initially differentiated for 3 days in neurobasal medium supplemented with B27, glutamax (Thermo Fisher Scientific), 10 μM retinoic acid (Sigma-Aldrich), and 50 ng/mL brain-derived neurotrophic factor (BDNF; Peprotech). The medium was then renewed in the presence of the indicated concentration of drugs. All drugs were dissolved in DMSO, and controls were treated with DMSO in parallel. After 3 days, supernatants were stored at − 80 °C for Aβ measurement, and cells were incubated for 1 h in the presence of 3-(4,5-dimethylthiazol-2-yl)-2,5-diphenyltetrazolium bromide (MTT) and then lysed in DMSO to check viability. For the assays on 7PA2 cells, 1.4×10^5 cells were seeded in 24-well plates. The day after, medium was replaced with the indicated concentration of compounds in DMEM without FBS supplement. Cells were incubated for further 24 h before medium was collected and stored at − 80 °C until Aβ quantification.

Aβ quantification

Aβ peptides were quantified with the Human β Amyloid (1-40) ELISA Kit Wako, Human β Amyloid (1-42) ELISA Kit Wako, and the Human β Amyloid (1-42) ELISA Kit, High-Sensitive (FUJIFILM Wako Pure Chemical Corporation), following the manufacturer's instructions.

Proximity ligation assay

Duolink proximity ligation assay (PLA) reagents were purchased from Sigma-Aldrich. Differentiated SH-SY5Y cells grown in slides were fixed and permeabilized with 0.3% Triton, 2% BSA in TBS-T (all from Sigma-Aldrich). The protocol recommended by the manufacturer was followed. Primary antibodies anti-Aβ (1-16) (Clone 6E10, 1:100, #803001, BioLegend) and anti-(human)-SYT11 (1:100, ab204589, Abcam) were used. Specificity of the anti-SYT11 antibody was assessed by western blot (Additional File 1: Fig. S8c). Images were acquired using a Zeiss LSM 780 Upright confocal, multiphoton FLIM system. For quantification, the positive dots were measured using Fiji ImageJ software. The number of cells was manually evaluated and results were expressed as the number of dots per cell.

Drugs/compounds

BACE inhibitor AZD3839, etodolac, fenoprofen, and pargyline were supplied by Selleckchem. Dexketoprofen and penbutolol were from Medchemexpress. Bendroflumethiazide was obtained from Sigma-Aldrich.

Animals and drug treatments

The homozygous 3xTg-AD mice and the corresponding wild-type mice (C57BL/6 × 129/Sv mixed background) were obtained from The Jackson Laboratory. Heterozygous $App^{wt/NL\text{-}F}$ and $App^{wt/NL\text{-}G\text{-}F}$ mice were obtained from the RIKEN Brain Science Institute and used to start colonies of homozygous $App^{NL\text{-}F}$ and $App^{NL\text{-}G\text{-}F}$ mice and their respective wild-type counterparts. Mice were maintained at the animal facility of the Barcelona Institute of Science and Technology, Barcelona, Spain. Only female animals were used in the study, as several lines of evidence suggest that pathology is stronger in 3xTg-AD female mice (https://www.jax.org/strain/004807). To allow comparison between models, only female mice were used in all the models.

Mice were maintained under standard housing conditions on a 12 h light/dark cycle, with water and food ad libitum. Genotyping was done on genomic DNA from the tail or ear, using standard PCR amplification and gel electrophoresis. The DNA primers (Sigma-Aldrich) used for genotyping are listed in Additional File 1: Table S7.

During the treatment period, 5-mo. $App^{NL\text{-}G\text{-}F}$ mice received a daily intraperitoneal injection of the indicated drugs for 4 weeks. Etodolac (50 mg/kg), dexketoprofen (15 mg/kg), fenoprofen (50 mg/kg), and bendroflumethiazide (20 mg/kg) were dissolved in a mixture of 5%Tween-80 (Sigma-Aldrich), 25% propylene glycol (Sigma-Aldrich), 25% Poly(ethylene glycol) (Sigma-Aldrich), and 45% phosphate-buffered saline (PBS). Penbutolol (20 mg/kg) and pargyline (20 mg/kg) were dissolved in PBS (veh.2). The drug doses were chosen according

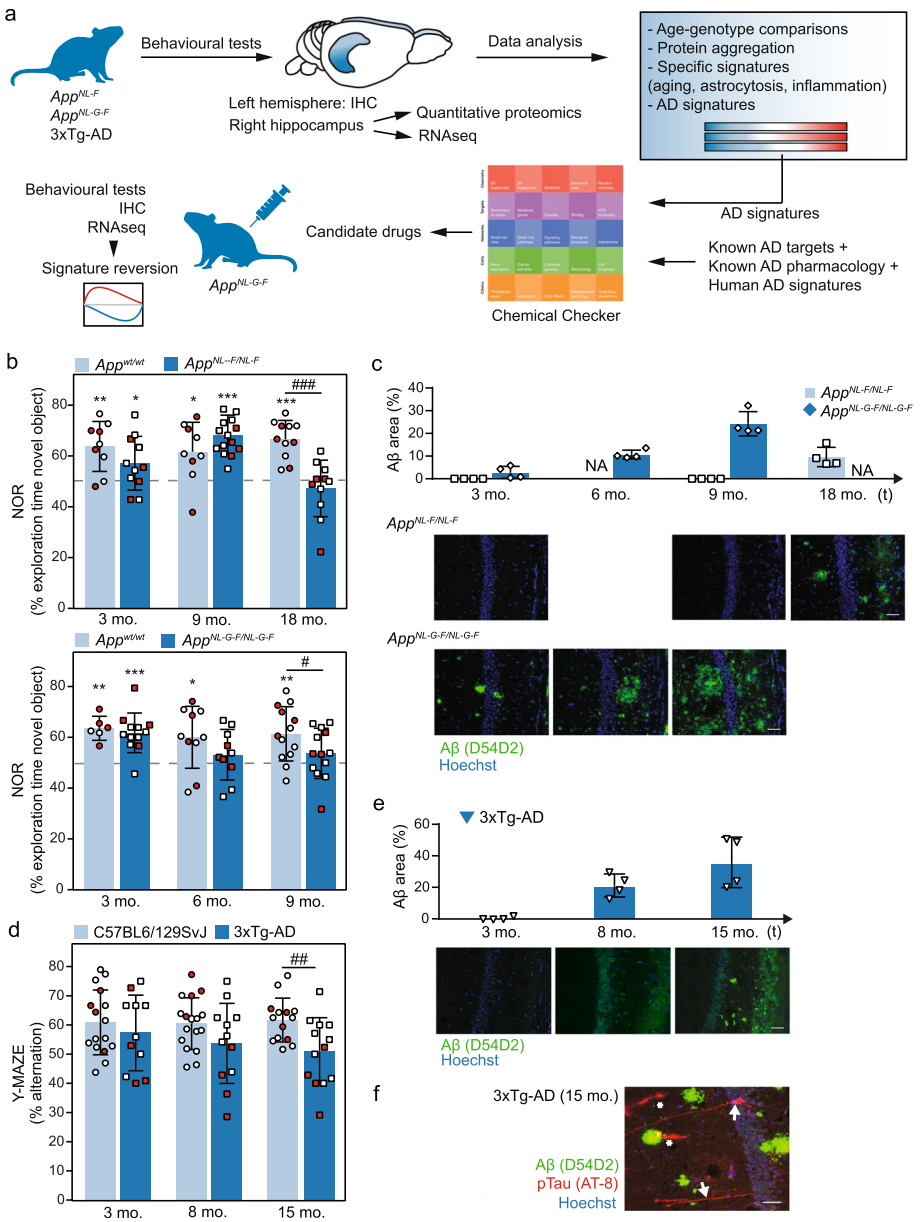

Fig. 1 Behavioral and histological characterization of mouse AD models. **a** Experimental flowchart. **b** Top, novel object recognition (NOR) test performed on *App*^{wt} (light blue; 3 mo. *n* = 9; 9 mo. *n* = 9; 18 mo. *n* = 11) and *App*$^{NL-F}$ (dark blue; 3 mo. *n* = 11; 9 mo. *n* = 15; 18 mo. *n* = 11) mice. Bottom, NOR test performed on *App*^{wt} (light blue; 3 mo *n* = 6; 6 mo *n* = 10; 9 mo *n* = 13) and *App*$^{NL-G-F}$ (dark blue; 3 mo *n* = 12; 6 mo *n* = 10; 9 mo *n* = 13) mice. Mean ± SD of the % of time exploring the novel object is shown. One-sample *t*-test versus a hypothetical value of 50 (* *p* value < 0.05, ** *p* value < 0.005, *** *p* value < 0.0005) and unpaired Student's *t* test (# *p* value < 0.05; ### *p* value < 0.0005) analysis are shown. Red dots indicate the results of the animals selected for histological and molecular profiling analyses. **c** Quantification and representative microphotographs of the CA1 region of the hippocampus of brain sections from 3-, 9-, and 18-mo. *App*$^{NL-F}$ mice or from 3-, 6-, and 9-mo. *App*$^{NL-G-F}$ mice stained with an anti-Aβ antibody (green) and Hoechst dye (blue) (*n* = 4 for each condition). Scale bars represent 50 μm. Photographs for both models were taken under identical conditions and the percentage of area with Aβ-positive staining was quantified as indicated in the "Methods" section. Mean ± SD of *App*$^{NL-F}$ (light blue) and *App*$^{NL-G-F}$ (dark blue) mice are shown. NA: not available. **d** Y-maze test performed on mixed non-transgenic C57BL6/129SvJ mice (light blue; 3 mo. *n* = 16; 8 mo. *n* = 17; 15 mo. *n* = 14) and 3xTg-AD transgenic mice (dark blue; 3 mo. *n* = 11; 8 mo. *n* = 12; 15 mo. *n* = 13). Mean ± SD of the % of alternation are shown. Unpaired Student's *t* test was performed (## *p* value < 0.05). Red dots indicate the results of the animals selected for histological and molecular profiling analyses. **e** As in **a**, sections from 3-, 8-, and 15-mo. 3xTg-AD mice were stained with an anti-Aβ antibody (green) and Hoechst dye (blue) (*n* = 4 for each condition). Scale bars represent 50 μm. Mean ± SD are shown. **f** Representative staining of Aβ (green), phosphorylated Tau (red), and nuclei (blue) in a brain section of a 15-mo. 3xTg-AD mouse (*n* = 4). White arrows indicate neurons with aggregated phosphorylated Tau. Asterisks indicate non-specific staining. Scale bar represents 50 μm

to previous publications on these compounds or similar compounds [26–31]. Groups of App^{wt} and App^{NL-G-F} mice were also treated with the vehicles.

Cognitive tests

The Novel Object Recognition (NOR) test was performed following the protocol described in [32]. On the first day, the habituation session, mice were placed in the empty box and allowed to explore for 5 min. Twenty-four hours after habituation, mice were placed in the same box in the presence of two identical objects (familiarization session) and allowed to explore for 10 min. The pair of objects was randomized and counterbalanced between mice. Twenty-four hours later (test session), mice were placed in the same box, but a novel object substituted one of the known objects, and the mice were allowed to explore for 5 or 10 min. The position of the novel object (left or right) was randomized and counterbalanced between mice. The objects and the box were cleaned with odorless soap between trials. All sessions were recorded. Object exploration was defined as the mouse sniffing or touching the object with the nose while looking at it. Climbing onto the object or chewing was not considered exploration. An experimenter blinded to the mouse condition tested assessed the exploratory activity manually. The amount of time exploring the novel object was expressed as a percentage of the total exploration time. Ability to discriminate the novel object was evaluated by performing a one-sample *t*-test against a hypothetical value of 50%.

The Y-maze test was conducted as described in [33]. The Y-maze apparatus consisted of three identical arms set at angles of 120°. Each animal was placed at the center of the maze and was allowed to explore it freely for 5 min. The maze was cleaned with odorless soap between trials. All sessions were recorded. The four paws of the mouse had to enter an arm to count as an arm entry. Alternation behavior was defined as consecutive entries into each of the three arms without repetition (ABC, CBA, etc.). We expressed the results as the percentage of spontaneous alternations, which was calculated by dividing the number of alternations by the total number of possible alternations (total arm entries − 2) × 100.

The following number of mice of the three AD models and the corresponding wild-type animals were used for behavioral characterization: C57BL6/129SvJ mice (3 mo. n = 16; 8 mo. n = 17; 15 mo. n = 14) and 3xTg-AD transgenic mice (3 mo. n = 11; 8 mo. n = 12; 15 mo. n = 13); App^{wt} (3 mo. n = 9; 9 mo. n = 9; 18 mo. n = 11) and App^{NL-F} (3 mo. n = 11; 9 mo. n = 15; 18 mo. n = 11) mice; App^{wt} (3 mo n = 6; 6 mo n = 10; 9 mo n = 13), and App^{NL-G-F} (3 mo n = 12; 6 mo n = 10; 9 mo n = 13). In the drug treatments, n = 4–7 App^{NL-G-F} mice and the corresponding wild-type were used.

Additional analyses of the videos were performed with dedicated tracking software (SMART video tracking, Panlab). The results obtained were in concordance with our observations. However, the inability of the software to discriminate between mouse head and tail in all the situations led us to rely on manual analysis for a more accurate result.

For further analyses, we manually selected the mice taking into account the results in order to maximize the chances to see differences with the controls. For the mice undergoing drug treatments, we selected the closest animals to the average response as observed in Fig. 5b, although the sample quality (incomplete perfusion of the sample, for example) was also a factor to take into account.

Mouse brain tissue preparation

Mice were anesthetized with an intraperitoneal (i.p.) mixture of ketamine/xylazine (100/10 mg/kg) and perfused intracardially with 0.9% saline solution. Brains were removed and cut in two hemispheres. The left hemisphere was snap-frozen in cold isopentane for 1 min, saved in dry ice, and stored at − 80 °C for immunofluorescence assays. The right hemisphere was dissected into the hippocampus and cortex. Only hippocampal tissue was used for analysis. Briefly, hippocampi from the same animal was minced and split in two halves, one for RNA extraction and the other for protein extraction, and snap-frozen in dry ice, and stored at − 80 °C (n = 4 per genotype and age). From the App^{NL-G-F} mice and the corresponding wild-type mice used for drug treatments, only RNA extraction from hippocampi was performed (n = 4 mice per condition).

Immunofluorescence staining

Twenty-micrometer coronal sections of the entire brain were cut using a Leica CM1900 cryostat. Sections were mounted on SuperFrost Ultra Plus slides (TermoFisher) and fixed in cold acetone for 10 min at room temperature (RT). After drying at RT, the mounted slides were saved at − 20 °C until further processing. Brain sections were washed in PBS for 5 min and incubated with blocking buffer (1% BSA, 5% goat serum, and 0.2% Triton in PBS) for 20 min at RT in a humidifier chamber. After the slides had been washed in PBS, the sections were incubated overnight at 4 °C with the primary antibodies diluted in PBS with 1% BSA and 0.2% Triton. The following primary antibodies were used: anti-Aβ (clone D54D2, 1:100, #8243, Cell Signaling), anti-human PHF-tau (clone AT-8, 1:100, #90206, Innogenetics), anti-Aβ (1-16) (Clone 6E10, 1:100, #803001, BioLegend), anti-Syt11 (1:100, #270003, Synaptic

Systems), or anti-Ifit3/P60 (1:50, ab76818, Abcam). After PBS washes, sections were incubated for 1 h at RT with the corresponding goat anti-rabbit Alexa Fluor 488 (1:250, Thermo Fisher), donkey anti-rabbit Alexa Fluor 647 (1:250, Thermo Fisher), or goat anti-mouse Alexa Fluor 568 (1:250, Thermo Fisher) diluted in PBS with 1% BSA and 0.2% Triton. Sections were counterstained with 2 μg/ml Hoechst for 5 min at RT, washed in PBS, and finally coverslipped using Fluoromount-G (EMS). Control sections (without primary antibody) were used to differentiate specific from non-specific staining. Images were acquired using a Nikon Eclipse E800M microscope equipped with an Olympus DP72 camera or a Zeiss LSM 780 Upright confocal, multiphoton FLIM system. For quantification, two coronal sections from $n = 4$ mice per group were analyzed, and the immunoreactive areas were measured using Fiji ImageJ software.

RNA extraction, mRNA library preparation, and sequencing

Total RNA was extracted from mouse hippocampal samples using a RNeasy Mini kit (Qiagen), following the manufacturer's protocol, and sent for whole transcriptome sequencing at the Centro Nacional de Análisis Genómico (CNAG-CRG). Total RNA was assayed for quantity and quality using the Qubit RNA BR Assay kit (Thermo Fisher Scientific) and RNA 6000 Nano Assay on a Bioanalyzer 2100 (Agilent).

The RNA-Seq libraries were prepared from total RNA using KAPA Stranded mRNA-Seq Kit Illumina Platforms (Roche-Kapa Biosystems) with minor modifications. Briefly, after poly-A-based mRNA enrichment with oligo-dT magnetic beads and 500 ng of total RNA as the input material, the mRNA was fragmented (resulting RNA fragment size was 80–250 nt, with the major peak at 130 nt). First-strand cDNA was synthesized using random priming. Second-strand cDNA was synthesized in the presence of dUTP instead of dTTP, to achieve strand specificity. The blunt-ended double-stranded cDNA was 3′ adenylated and Illumina indexed adapters (Illumina) were ligated. The ligation product was enriched with 15 PCR cycles and the final library was validated on an Agilent 2100 Bioanalyzer with the DNA 7500 assay.

Each library was paired-end sequenced using TruSeq SBS Kit v4-HS, with a read length of 2 × 76bp. On average, we generated 53 million paired-end reads for each of the 48 samples of $App^{NL\text{-}G\text{-}F}$, $App^{NL\text{-}G\text{-}F}$, App^{wt} mice, and 80 million reads for each of the 24 samples of 3xTg-AD and C57BL/6 × 129/Sv mice in a fraction of a sequencing lane on HiSeq2000 (Illumina, Inc.) following the manufacturer's protocol. Image analysis, base calling, and quality scoring of the run were processed using the manufacturer's software Real-Time Analysis (RTA 1.18.64) and followed by generation of FASTQ sequence files by CASAVA.

RNA-Seq data analysis

STAR software (Dobin et al., 2013) was used to align the raw RNAseq reads to the mouse reference genome (GRCm38/mm10 and GENCODE vM15 genome annotations [34]). MAPT, PSEN1, and humanized APP and/or mutated sequences were included according to the genotype of the mouse model analyzed. We used casper [35] to quantify the expression of all transcript isoforms, which were aggregated at gene level and quantile-normalized. To reduce biases caused by low expression, we considered only genes with at least 0.2 RPKMs in 90% of the samples. This filter was applied separately to the 48 samples of APP knock-in mice and their controls (GSE168430), to the 24 samples of 3xTg mice and their controls (GSE168428), and to the 32 samples of drug- or vehicle-treated mice (GSE168429). We used the Limma package [36] to perform differential expression analysis based on empirical Bayes moderated *t*-statistics, including experimental batch as covariate. We performed all pairwise comparisons along the genotype- and time-axes to describe AD progression and physiological aging. To derive the *AD signatures*, we specified an additional model to analyze the APP knock-in dataset, in which we considered age as a continuous variable together with its interaction with genotype. These models were used to estimate the linear association of gene expression with age for each genotype. Multiple comparisons correction was performed using the Benjamini-Hochberg algorithm. For visualization purposes, quantile-normalized expression values were corrected by batch using the removeBatchEffect function from Limma. Genes were ranked by multiplying their fold change sign by the − log10 (*p* value) for pre-ranked GSEA [37]. We used the prcomp function in R to perform a principal components analysis (PCA) of the gene expression matrices before and after batch adjustment. We used the pvca Bioconductor package to perform a principal variance component analysis (PVCA) aimed at identifying the most prominent sources of variability *n* each dataset.

Mass spectrometry sample preparation

Frozen mouse hippocampi were homogenized in 0.2 ml of pre-cooled homogenization buffer (0.3 M sucrose, 10 mM MOPSNaOH, and 1 mM EDTA) supplemented with complete protease inhibitor cocktail (Roche). In total, 50 μl of lysis buffer (8% SDS and 0.2 M DTT in 0.2 M Tris-HCl pH 7.6) was added to 50 μl homogenate and the mixture was incubated for 3 min at 95 °C. Once cooled, the total protein extracts were stored at − 20 °C until quantification. Protein samples were quantified using the Pierce 660 Protein Assay Kit, reduced with tris (2-carboxyethyl) phosphine (TCEP), alkylated, and digested with trypsin. After digestion, all samples were isotopically labeled with the corresponding iTRAQ-8plex

reagent according to the experimental design and following the manufacturer's instructions (Thermo Fisher Scientific). iTRAQ labels were randomized, minimizing the co-occurrence of labels within a biological condition. Samples were desalted using C18 and strong cationic exchange tips. Each batch was fractionated off-line by basic reversed-phase chromatography. Sample fractionation was performed with a Zorbax 300 Extend-C18 column (2.1 × 150 mm, 3.5 mm) in an AKTA micro ETTAN gradient LC system (Amersham Biosciences).

Peptides were separated in a total of 84 collected fractions and grouped into 24 fraction groups per batch and dried via vacuum centrifugation. Fraction groups (~ 5 μg) were reconstituted in 48 μl of 3% acetonitrile (ACN) and 1% formic acid (FA) aqueous solution for nano LC-MS/MS analysis.

Mass spectrometry analysis

Mass spectrometry data were collected on an Orbitrap Fusion Lumos™ Tribrid mass spectrometer (Thermo Scientific) equipped with a Thermo Scientific Dionex Ultimate 3000 ultrahigh pressure chromatographic system (Thermo Fisher Scientific) and an Advion TriVersa NanoMate (Advion Inc. Biosciences) as the nanospray interface. Peptide mixtures (6 μl) were loaded into a μ-Precolumn (300 μm i.d × 5 mm, C18 PepMap100, 5 μm, 100 Å, C18 Trap column; Thermo Fisher Scientific) at a flow rate of 15 μL/min and separated using a C18 analytical column (Acclaim PepMap TM RSLC: 75 μm × 75 cm, C18 2 m, nanoViper) with a flow rate of 200 nl/min and a 210 min run, comprising three consecutive steps with linear gradients from 1 to 35% B in 180 min, from 35 to 50% B in 5 min, and from 50 to 85% B in 2 min, followed by isocratic elution at 85% B in 5 min and stabilization to initial conditions (A = 0.1% FA in water, B = 0.1% FA in ACN). The mass spectrometer was operated in a data-dependent acquisition (DDA) mode. In each data collection cycle, one full MS scan (400–1600 m/z) was acquired in the Orbitrap (120 k resolution setting and automatic gain control (AGC) of 2×10^5). The following MS2-MS3 analysis was conducted with a top-speed approach. The most abundant ions were selected for fragmentation by collision-induced dissociation (CID). CID was performed with collision energy of 35%, 0.25 activation Q, an AGC target of 1×10^4, an isolation window of 0.7 Da, a maximum ion accumulation time of 50 ms, and turbo ion scan rate. Previously analyzed precursor ions were dynamically excluded for 30 s. For the MS3 analyses for iTRAQ quantification, multiple fragment ions from the previous MS2 scan (SPS ions) were co-selected and fragmented by HCD using a 65% collision energy and a precursor isolation window of 2 Da. Reporter ions were detected using the Orbitrap with a resolution of 30 k, an AGC of 1×10^5 and a maximum ion accumulation time of 120 ms. Spray voltage in the NanoMate source was set to 1.60 kV. RF Lens were tuned to 30%. The minimal signal required to trigger MS to MS/MS switch was set to 5000. The mass spectrometer was working in positive polarity mode and single charge state precursors were rejected for fragmentation.

Database searches were performed with Proteome Discoverer v2.1.0.81 software (Thermo Fisher Scientific) using Sequest HT search engine and SwissProt Mouse_canonical_2016_11 including contaminants and MAPT, PSEN1, and APP humanized and/or mutated sequences according to each of the mouse models analyzed. Search was run against targeted and decoy database to determine the false discovery rate (FDR). Search parameters included trypsin, allowing for two missed cleavage sites, carbamidomethyl in cysteine and iTRAQ 8-plex peptide N-terminus as static modification and iTRAQ 8plex in K/Y, methionine oxidation and acetylation in protein N-terminus as dynamic modifications. Peptide mass tolerance was set to 10 ppm and the MS/MS tolerance to 0.6 Da. Peptides with an FDR < 1% were considered as positive identifications with a high confidence level. The mass spectrometry proteomics data have been deposited to the ProteomeXchange Consortium via the PRIDE [38] partner repository with the dataset identifier PXD024538.

All computations were performed in the R statistics framework. The iTRAQ reporter intensities were filtered by contamination flag set to "False," average reporter signal to noise ratio larger than 3, intensity value larger than 1000, and the Peptide Quan Usage flag set to "Use." For peptides without a unique assigned protein, the protein with maximum total intensity was defined as master protein. Filtered intensities were normalized within each processing batch by a size factor computed as in [39]. To do this, intensities were summarized via the median for each protein and sample. A reference sample was computed as the mean value of all samples for each protein. Size factors were computed as the median ratio of each protein against the reference sample. Once the size factors were obtained, all PMSs were divided by the corresponding factor and the log2 value (after adding 1) was computed.

For each protein, a linear model was fitted with or without random effects depending on the number and combination of peptides measured in each age*genotype group. When more than one peptide was measured in more than one group and throughout several fractions, peptide, fraction (within peptide), and sample were included in the model as random effects, with age × genotype and batch as fixed effects. When only one peptide or one fraction was found, random effects were dropped accordingly. When no repeated measures existed for a given protein, a linear model was fitted with the same fixed effects. Mixed effects models were fitted using the lmer function from the lme4 package [40], while linear

models were fitted with the lm function of the stats package. To perform the desired contrasts, the glht function from the multcomp package was used without p value adjustment [41]. Multiple comparisons correction was performed a posteriori for each contrast using the p.adjust function with the Benjamini-Hochberg method.

For visualization purposes, normalized intensities were corrected by peptide, sample, and batch using the model coefficients.

Statistics

Data were analyzed with the Prism statistical package. Unless otherwise indicated in the figure legend, P values were calculated using an unpaired, one-tailed, Student t test. To control possible batch effects in transcriptomics and proteomics, we used a blocked/randomized design. Biological replicates were confounded with the processing batches (4 batches in each mouse model). iTRAQ labels were randomized to minimize the co-occurrence of labels within a biological condition.

Virtual signature-based screening of compounds

We devised a strategy to select the most promising small molecules to modify the biology of AD within the universe of the ~ 1 M bioactive compounds cataloged in the CC. The CC aggregates 25 data types for the molecules, organized in five levels (A-E) and sublevels (1-5). On the one hand, we defined three "pharmacological queries" to identify compounds that were (1) chemically similar (p value < 0.001 in the A1-5 bioactivity spaces of the CC) to drugs that have entered clinical trials against AD or that shared a significant number of targets with them (B4 signatures). More specifically, we considered drugs thought to target amyloid fibrils and plaques, tau, cholesterol, inflammation, neurotransmitters, and cholinergic receptors [42]. We also (2) selected small molecules that showed similar transcriptional (D1) or cell sensitivity (D2) to these drugs. In addition, (3) we looked for small molecules known to bind putative AD targets, as defined by OpenTargets [43]. Furthermore, we designed two "biological queries" to capture connectivities between the discovered molecular changes in AD models and the bioactivity data available in the CC. In particular, we looked for (4) compounds that trigger transcriptional responses able to neutralize the changes observed in the AD mice in the CC D1 space. Finally, (5) we used the LINCS L1000 resource [44] to find perturbation experiments, mainly shRNA, that could also revert our AD transcriptional signatures, used them as putative AD targets and looked for compounds in the CC able to inhibit their activity (B spaces). Molecules selected in at least one of the 5 queries were kept; these candidates based on virtual screening can be found in Additional File 2: Table S5, together with detailed scores for each of the queries. Scores are represented as empirical − log10 p values obtained over the CC universe of > 800 k molecules.

Additional calculations were done to facilitate the selection of compounds for experimental screening. In particular, we trained machine-learning classifiers based on the BBBP and BACE datasets available from MoleculeNet [45], and Aβ40, Aβ42, and Aβ40/Aβ42 ratio from a previous compound screening performed in iPSC cells [46] (binarization cut-offs: Aβ 0.8, ratio 0.9). As a machine-learning method, we used an ensemble-based approach (extra-trees classifiers) and, as features, we used CC signatures. Ensemble-based methods applied to CC signatures have shown exceptional performance across a wide range of benchmarking tasks [47]. In a stratified 5-fold cross-validation, we obtained ROC AUC > 0.918, 0.874, 0.774, 0.690, and 0.874 for BBP, BACE, Aβ40, Aβ42, and Aβ ratio models, respectively.

Results

Characterization of cognitive impairment in three AD mouse models

To gain an understanding of the dynamics of AD progression, we characterized different AD mouse models at the phenotypic and molecular levels, at three representative stages of the disease (onset, progression and advanced). As primary models, we used two *App* mutated knock-in mouse versions widely used in AD preclinical research and developed to avoid potential artifacts of transgene overexpression [48]. $App^{NL\text{-}F}$ and $App^{NL\text{-}G\text{-}F}$ mice contain a humanized Aβ sequence with the Swedish "NL" (KM670/671NL) and Beyreuther/Iberian "F" (I716F) mutations. In addition, the $App^{NL\text{-}G\text{-}F}$ model contains the Arctic mutation "G" (E693G) in the Aβ sequence [49]. To complement these models, we also characterized the classical 3xTg-AD mice, which overexpress mutated human APP ($APP^{KM670/671NL}$) and Tau ($MAPT^{P301L}$) proteins in a $Psen1^{M146V/M146V}$ background [50].

To determine the disease stage in each AD model, we first evaluated the cognitive status of $App^{NL\text{-}F}$ and $App^{NL\text{-}G\text{-}F}$ mice of different ages using the novel object recognition (NOR) test, which is substantiated in the innate preference of mice for novelty (i.e., if the mouse recognizes a familiar object, it will spend most of its time exploring the novel object) [32]. We used 3-, 9-, and 18-month-old (mo.) $App^{NL\text{-}F}$ mice and 3-, 6-, and 9-mo. $App^{NL\text{-}G\text{-}F}$ mice as representatives of different disease stages [49]. We found that 18-mo. $App^{NL\text{-}F}$ mice spent a similar time exploring the novel object and familiar object (47.3 ± 11.1%), while their App^{wt} counterparts spent 66.6 ± 7.5% of time exploring the novel object. Younger $App^{NL\text{-}F}$ mice (i.e., 3 and 9 mo.) did not show significant differences in object exploration time,

thereby confirming that this AD model has memory defects only at advanced ages (Fig. 1b). In the case of the $App^{NL\text{-}G\text{-}F}$ mice, 6- and 9-mo. animals were not able to discriminate the novel object (53.2 ± 9.9% and 53.7 ± 9.9%, respectively), thereby indicating earlier cognitive impairment than the $App^{NL\text{-}F}$ mice (Fig. 1b). As expected, App^{wt} animals spent more time on the novel object at all the ages tested (63.6 ± 4.7%, 60.0 ± 12.2% and 61.4 ± 10.7% in 3-, 6-, and 9-mo. mice, respectively).

We next selected samples of representative female mice (shown in red in Fig. 1b; see "Methods" for details) and quantified the Aβ aggregates in the hippocampal region of the two knock-in models (Fig. 1c). We observed that 18-mo. $App^{NL\text{-}F}$ mice presented small plaques with an Aβ-positive area of 9.6 ± 4.3%, whereas 3- and 9-mo. $App^{NL\text{-}F}$ mice did not show significant Aβ area staining. On the other hand, all 3-, 6-, and 9-mo. $App^{NL\text{-}G\text{-}F}$ mice showed a progressive increase in Aβ staining (2.8 ± 2.6%, 10.7 ± 1.9%, and 24.3 ± 5.3%, respectively). As expected, the corresponding App^{wt} mice did not show Aβ staining (data not shown). Overall, these results were in line with the initial characterization of these mouse models [49], and comparison of hippocampus Aβ plaque accumulation with the results of the NOR test (Fig. 1b) pointed to the presence of a threshold of Aβ pathology from which these mice start to develop cognitive impairment (18 months for $App^{NL\text{-}F}$ mice and 6 months for $App^{NL\text{-}G\text{-}F}$ mice).

To complement the two knock-in models, we also characterized cognitive status (Fig. 1d) and Aβ plaque formation (Fig. 1e) in 3-, 8-, and 15-mo. 3xTg-AD mice in a Y-maze spontaneous alternation experiment, which also evaluates hippocampal defects by measuring the willingness of mice to explore new environments. As expected, 8- and 15-mo. 3xTg-AD mice showed a progressively reduced percentage of alternation in the Y-maze (53.7 ± 13.7% and 50.9 ± 11.6%, respectively) compared with wild-type controls, which showed around 60% of alternation at all ages (Fig. 1d), suggesting cognitive impairment of the former. Although intracellular staining of Aβ was detected at 8 months, dense Aβ plaques were only clearly visible at 15 months of age (Fig. 1e). Note that the 3xTg-AD model has the unique characteristic of the concomitant manifestation of both plaques and tangles at late ages due to the overexpression of a mutated form of Tau ($MAPT^{P301L}$). Indeed, we confirmed the presence of intracellular hyper-phosphorylated Tau in neurons of 15-mo. mice (Fig. 1f).

Characterization of the gene expression and protein abundance associated with AD

To identify molecular changes associated with these pathological features, we performed a comprehensive parallel quantification of gene expression levels and protein abundance in the dissected hippocampi of the $App^{NL\text{-}F}$, $App^{NL\text{-}G\text{-}F}$, and 3xTg-AD mice previously analyzed. More specifically, the right hippocampus of each mouse was minced and split in two parts, one for RNA sequencing, and the other part for proteomics studies. We used the hippocampi of 3-, 9-, and 18-mo. $App^{NL\text{-}F}$ mice; 3-, 6-, and 9-mo. $App^{NL\text{-}G\text{-}F}$ mice; and 3-, 8-, and 15-mo. 3xTg-AD mice (n = 4 per genotype and time point), together with the corresponding App^{wt} and C57BL6/129SvJ controls. Overall, we measured the expression levels of 21,950 protein-coding genes. We also performed proteomic studies, based on the 8-plex iTRAQ labeling method [51] and LC-MS/MS, and we were able to quantify a total of 8732 unique protein groups, corresponding to 6837, 7938, and 7473 proteins from $App^{NL\text{-}F}$, $App^{NL\text{-}G\text{-}F}$, and 3xTg-AD mice, respectively. A detailed description of the protocols is provided in the "Methods" section, and the complete datasets are available in GEO [52] GSE168431 and PRIDE [38] PXD024538.

To identify the changes in transcriptional and protein abundance associated with each disease stage, we first performed a differential abundance analysis comparing the AD genotypes at indicated ages with their wild-type counterparts, applying several false discovery rate (FDR) thresholds (Fig. 2a). We also compared different ages within the same genotype to evaluate changes associated with disease progression for all three models (Fig. 2b). Consistent with the phenotypes described in Fig. 1, 6- and 9-mo. $App^{NL\text{-}G\text{-}F}$ mice showed the largest effects on gene/protein down- and, specially, upregulation (150 genes and 51 proteins for 6-mo. mice, and 295 genes and 64 proteins for 9-mo. mice; n = 4, FDR < 5% and |logFC| > 0.5 and 0.25). Interestingly, few changes were found in the 6- vs. 9-mo. comparison (Fig. 2b; 18 genes and 0 proteins; n = 4, FDR < 5% and |logFC| > 0.5 and 0.25). This observation thus indicates that most of the changes take place between 3 and 6 months of age, when Aβ plaques became more evident and cognitive impairment appeared (Fig. 1b, c). On the other hand, despite the small Aβ plaques observed in 3-mo. $App^{NL\text{-}G\text{-}F}$ mice (Fig. 1c), no detectable changes in transcript or protein abundance were observed with respect to their wild-type counterparts (Fig. 2a). Similarly, 18-mo. $App^{NL\text{-}F}$ mice did not show differences with their age-matched wild-type controls (Fig. 2a). However, an age comparison (Fig. 2b; 3- vs. 18-mo. $App^{NL\text{-}F}$) identified age-dependent differentially expressed genes/proteins (107 and 72, respectively; n = 4, FDR < 5% and |logFC| > 0.5 and 0.25). When analyzing the genotype-dependent changes in the 3xTg-AD model, we already observed significant gene expression and protein abundance differences at 3 months of age (Fig. 2a), even before the first signs of Aβ pathology appeared in the hippocampus of these mice

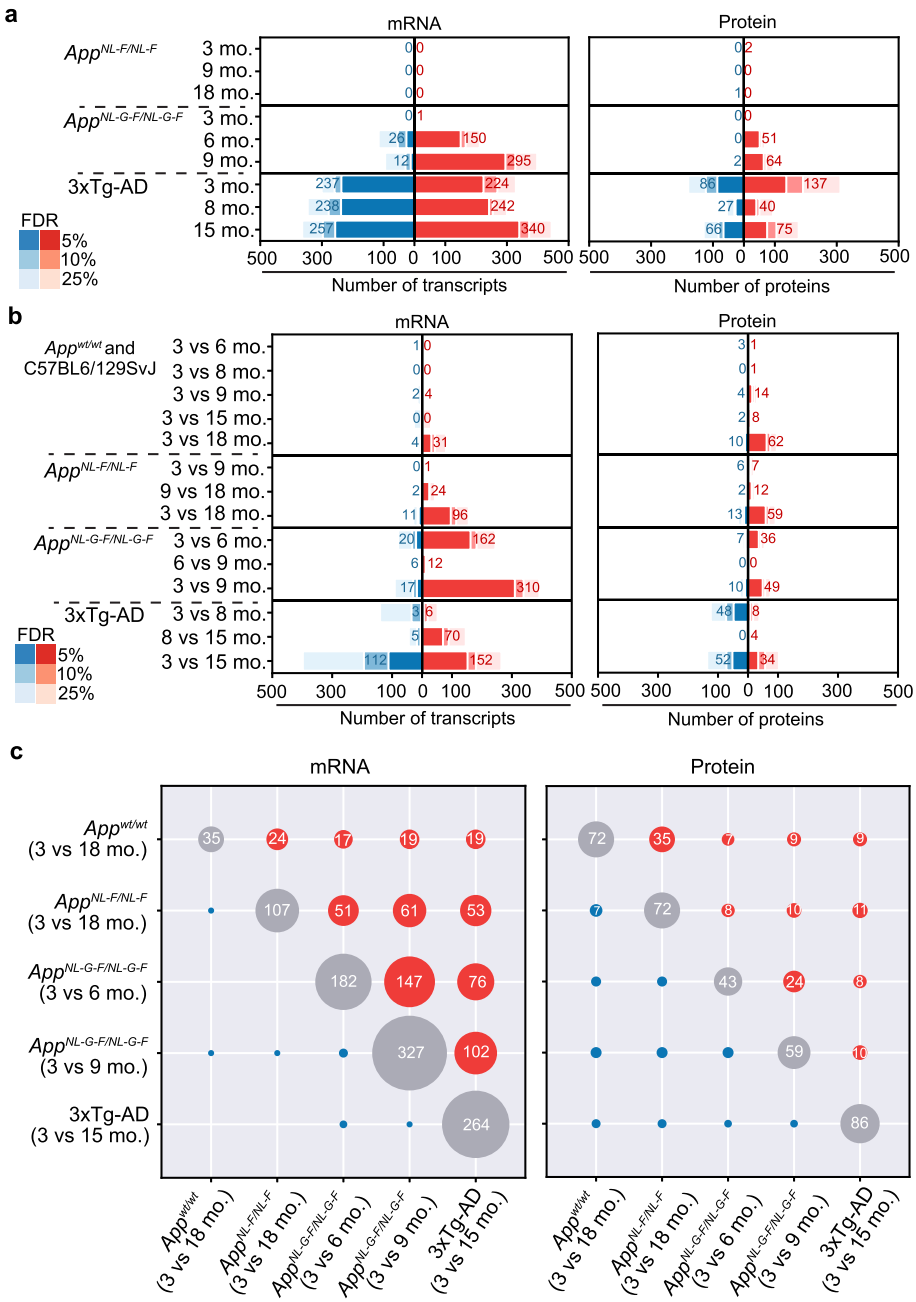

Fig. 2 Differential molecular profiling and AD progression. **a** Number of differentially expressed genes (left panel) and proteins (right panel) comparing the three mouse AD models (App^{NL-F}, App^{NL-G-F}, and 3xTg-AD) at different ages with their corresponding, age-matched, wild-type controls. Red and blue represent up- and downregulated genes/proteins, respectively. Bars indicate the number of significant genes/proteins that changed between conditions at different thresholds of false discovery rate (FDR) and with an absolute log fold change (LogFC) larger than 0.5 for mRNA and 0.25 for proteins. Numbers depicted in the figure correspond to FDR < 5%. $N = 4$ for all the conditions. **b** Number of differentially expressed genes (left panel) and proteins (right panel) comparing each genotype at the different ages. $N = 4$ for all the conditions. **c** Overlap between differentially expressed genes (left panel; absolute LogFC> 0.5, FDR < 5%) or proteins (right panel; absolute LogFC> 0.25, FDR < 5%) comparing AD mouse models and disease stages

(Fig. 1e). Moreover, in contrast to the App^{NL-G-F} model, the number of differentially expressed genes/proteins did not increase with disease progression (Fig. 2a). Indeed, a principal variance component analysis (PVCA) showed that the genotype accounted for 48% and 19% of the variance observed in the transcriptomics and proteomics data for this model, compared to the 17% and 13% observed in App^{NL-G-F} and the 8% and 4% observed in

App^{NL-F} models (Additional File 1: Fig. S1b). We attribute this effect to the wild-type controls used with the 3xTg-AD model, since one of the drawbacks of the 3xTg-AD model is that it has to be kept in a mixed background, as backcrossing may affect the initially reported phenotype [53]. Therefore, similar mixed background mice (as recommended by The Jackson Laboratory) were used as controls. This effect does not influence the comparisons across ages in the 3xTg-AD model, where we observed, as expected, an increase in dysregulated genes/proteins as AD advanced (Fig. 2b).

Interestingly, we observed a significant degree of overlap between the upregulated genes and proteins in the three different models, thereby suggesting that, despite the notable differences between models, there are common molecular patterns across them (Fig. 2c). For instance, the strongest overlap across models occurred between App^{NL-G-F} (3- vs. 9-mo.) and 3xTg-AD (3- vs. 15-mo.) mice, which shared 102 upregulated genes (odds ratio (OR) 247.53, Fisher's exact test p value 7.58×10^{-164}) and 10 proteins (OR 62.47, p value 6.45×10^{-14}). On the other hand, App^{NL-F} (3- vs. 18-mo.) also shared a significant number of upregulated genes and proteins with both App^{NL-G-F} (3- vs. 9-mo.), with 61 genes and 10 proteins (OR 172.13 and 29.22; p value 1.37×10^{-94} and 3.96×10^{-11}) and 3xTg-AD (3- vs. 18-mo.), with 53 genes and 11 proteins (OR 316.27 and 53.82; p value 1.12×10^{-95} and 1.99×10^{-14}). As for the downregulated genes and proteins, the changes were much less evident and specific for each model. Indeed, only 17 genes and 10 proteins were significantly downregulated in App^{NL-G-F} mice (3- vs. 9-mo.), and the only significant overlap between downregulated genes and proteins corresponded to the App^{NL-F} (3- vs. 18-mo.) and App^{wt} (3- vs. 18-mo.) mice, which involved 7 proteins (OR 2250.89 and p value 4.68×10^{-18}).

Additionally, analysis of the App^{wt} mice corresponding to the knock-in models allowed us to study the relationship between healthy aging and AD progression at the molecular level. Comparison of "old" (18-mo.) with "young" (3-mo.) wild-type mice revealed the upregulation of 31 genes and 62 proteins and the downregulation of 4 genes and 10 proteins (Fig. 2b; Additional File 2: Table S1; FDR < 5% and |logFC| > 0.5 and 0.25). At the transcriptional level, we detected the upregulation of known microglial markers such as *Cst7*, *Clec7a* or *Lyz2* (Additional File 1: Fig. S2a), thereby suggesting an increase in the inflammatory component in the aged hippocampus. This finding is in line with the recent characterization of gene expression in aged microglia at single-cell level [8, 54, 55], and also with the general accepted role of inflammation as one of the hallmarks of aging [56]. Of note, a significant number of these genes were also upregulated in other comparisons involving younger AD mice (e.g., 17 of the 21 genes were already upregulated in 3- vs. 6-mo. App^{NL-G-F} animals, OR 215.73 and p value 3.48×10^{-30}; Fig. 2c and Additional File 1: Fig. S2a), thereby suggesting that Aβ pathology promotes features of molecular aging. However, the observation that 18-mo. App^{wt} mice did not present cognitive deficits (Fig. 1c) confirms that AD is not merely accelerated aging, and some differences must exist with App^{NL-F} mice, which indeed showed cognitive impairment at 18 months of age (Fig. 1c) despite the lack of significantly altered genes or proteins (Fig. 2a). Direct comparison between App^{wt} (3- vs. 18-mo.) and App^{NL-F} (3- vs. 18-mo.) mice indicated a similar trend of up- and downregulated genes (Additional File 1: Fig. S2b), although we identified a set of genes with accentuated changes in App^{NL-F} mice (Additional File 2: Table S2). Among these, we found a number of chemokines (*Ccl6*, *Ccl3*, or *Ccl5*) and also markers of microglial activation (*Cd14*, *Tyrobp*). Interestingly, *Ccl3* has been found to impair mouse hippocampal synaptic transmission, plasticity and memory, and polymorphisms in this gene increase the risk of AD in humans [57].

While there was a significant overlap between the transcriptional changes in 3xTg-AD mice (3- vs. 15-mo.) and those observed in the App^{NL-G-F} model (76 with 3- vs. 6-mo. comparison; 102 with 3- vs. 9-mo. comparison; Fig. 2c), we would expect that some of the changes observed in the 3xTg-AD model could be attributed to the presence of Tau fibrils (Fig. 1f). Therefore, we directly compared changes in 3xTg-AD mice (3- vs. 15-mo.) with App^{NL-G-F} mice (3- vs. 9- mo.) to identify 3xTg-AD-specific changes (Additional File 1: Fig. S2c; Additional File 2: Table S3). The 3xTg-AD model showed an accentuated upregulation of *Klk6* and *Lcn2*, which have been evaluated as possible markers of AD and vascular dementia, respectively [58, 59]. We also observed an increased upregulation of Serpina3n protein, a serine protease inhibitor previously identified in human amyloid deposits [60] and dysregulated in prion diseases [61], which might indicate a role for Tau aggregates in the metabolism of these diseases. Additionally, we found the upregulation of *Alox12b*, which encodes a lipoxygenase enzyme, only in the 3xTg-AD model. This observation is consistent with recent findings in a Tau mouse model [62] and the potential role that lipoxygenases might have in Tau metabolism [63]. Of note, we consistently detected the downregulation of extracellular matrix genes (*Col1a2*, *Col3a1*) and proteins (Col6a1), as well as proteins linked to adhesion or actin function, such as Flna, Palld, or Fbln5 (Fig. 2c; Additional File 2: Table S3). These observations thus support the hypothesis that hyper-phosphorylated Tau compromises the integrity and function of the blood–brain barrier in the 3xTg-AD mouse model [64].

Physiological aging and AD progression

To gain further insight into the common molecular events that take place in response to pathogenic *App* mutations, we integrated the two *App* knock-in mouse models ($App^{NL\text{-}F}$ and $App^{NL\text{-}G\text{-}F}$) and their respective App^{wt} mice to analyze the entire experiment as a whole. To this end, and in order to capture the temporal dynamics of the transcriptional changes associated with physiological aging and AD progression, we considered the age of the animals as a continuous variable. We measured the linear association of gene expression with age for each genotype and identified a series of up- and downregulated genes in $App^{NL\text{-}G\text{-}F}$ mice with respect to App^{wt} that we named *AD signatures* (*AD-UP* and *AD-DW*, respectively; Additional File 2: Table S4). Finally, we compared the relative expression of AD signature genes across all the mouse models (Fig. 3a and Fig. 3c, left panels) and observed that a number of up- and downregulated genes followed similar trends in the comparisons of 3- vs. 15-mo. and 8- vs. 15-mo. 3xTg-AD mice (Fig. 3a, c, left panels). Indeed, the *AD signatures* derived from the *App* knock-in mice were significantly enriched in the 3xTg-AD transcriptional changes (Additional File 1: Fig. S3a), indicating that these signatures are common to the three AD models.

To assess the potential translatability of our AD signatures, we compared them to the transcriptional signatures of human AD identified at the Mount Sinai/JJ Peters VA Medical Center Brain Bank (MSBB-AD). Their transcriptomic analysis identified five AD molecular subtypes that can be grouped in three major classes. Classes A and B seem to be more vulnerable to synaptic excitation, whereas class C seems to be more vulnerable to synaptic depression [65]. The authors described an upregulation of immune-related pathways in subtypes B2, C2, and especially C1 compared to normal controls. This finding is indeed recapitulated in our AD mouse models and is reflected in the *AD-UP signature* (Additional File 1: Fig. S4). On the other hand, the authors describe a downregulation of glutaminergic, γ-aminobutyric acid (GABA) related, glycinergic, and dendritic synaptic pathways in class C subtypes. This

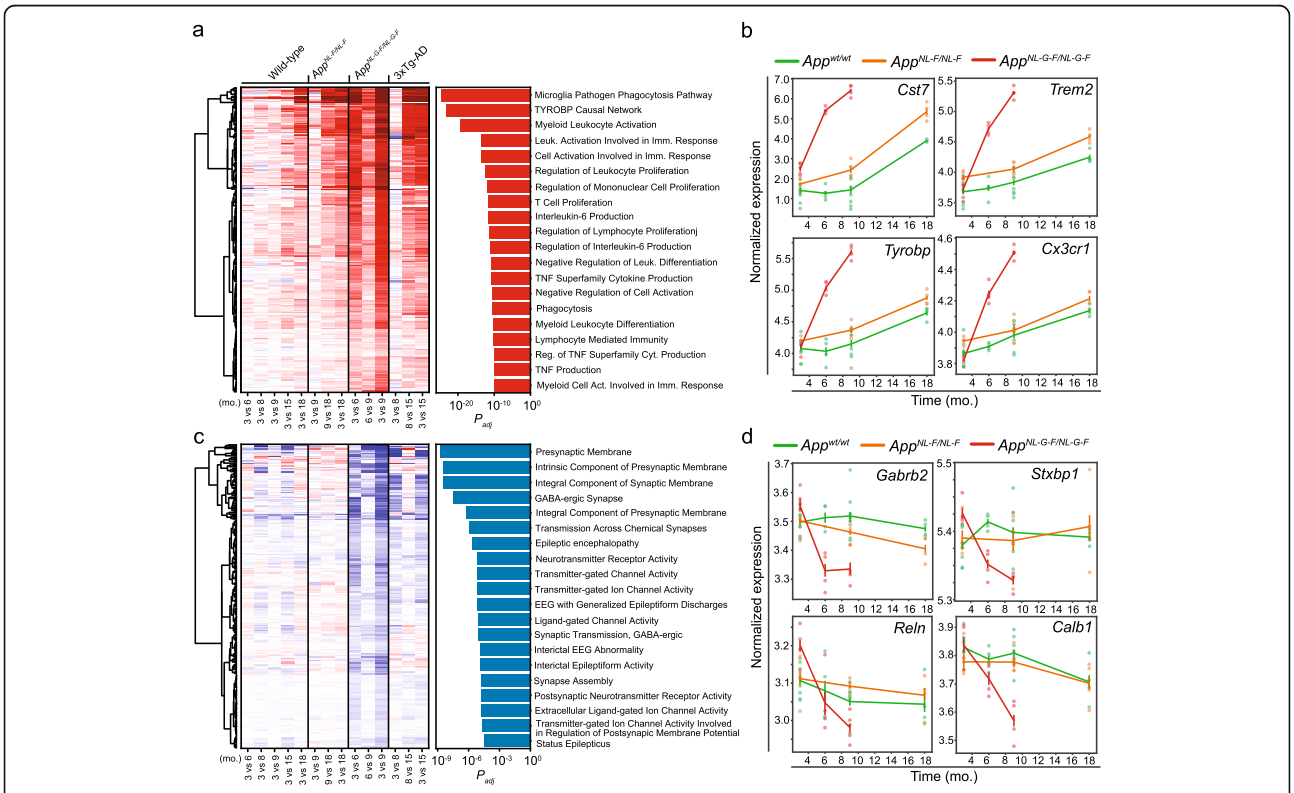

Fig. 3 Identification and functional annotation of AD signatures. **a** Heatmap showing the progression of the transcriptional changes in the top-250 genes showing a positive genotype by age interaction (*AD-UP signature*). Each gene is represented by a row of colored tiles, the color representing the RNA expression level for the indicated condition by column (red, upregulated; blue, downregulated). The bar plot on the right indicates the top-20 significant pathways corresponding to the functional enrichment analysis of these top-250 genes, indicating the adjusted *p* value on the *X*-axis. **b** Normalized gene expression at different time points expressed in months (mo.) for four examples of the *AD-UP signature* (*Cst7*, *Trem2*, *Tyrobp*, and *Cx3cr1*) in the $App^{NL\text{-}G\text{-}F}$ (red line), $App^{NL\text{-}F}$ (orange line), and App^{wt} (green line) mice. $N = 4$. **c** As in **a**, progression of the transcriptional changes in the top 250 genes showing a negative genotype by age interaction (*AD-DW signature*) and functional enrichment analysis of these genes. **d** As in b, four examples (*Gabrb2*, *Stxbp1*, *Reln*, and *Calb1*) of the *AD-DW signature* are shown. $N = 4$

phenotype is also recapitulated in our AD mouse models and reflected in the *AD-DW signature*. Note that the changes in the class A subtype (atypical) are opposite to the molecular changes observed in typical and intermediate subtypes (C and B) (Additional File 1: Fig. S5). Overall, our AD signatures could be useful to discriminate between case and controls of the typical C (especially C1) AD subtype, but the atypical and intermediate subtypes (A and B) would be out of the applicability domain. Moreover, we found that the derived AD signatures included 28 genes defined as AD risk factors in human genetic studies [66] (Odds ratio (OR) 3.16 and Fisher's exact test p val 6.29×10^{-7}), 23 of them in the *AD-UP signature* and 5 in the *AD-DW signature* (Additional File 1: Fig. S3b and Additional File 2: Table S4).

We performed a functional enrichment analysis of AD signatures and found that the top-20 upregulated pathways corresponded exclusively to the activation of the immune system, including phagocytosis or cytokine production pathways (Fig. 3a, right panel). Indeed, many of the top upregulated transcripts were directly associated with microglia activation (Fig. 3b), including *Tyrobp* and its putative receptor *Trem2*, whose variants are associated with an extraordinarily increased risk for AD in humans [67]. Our AD signatures also included 46 disease-associated microglia genes (46 of 382; OR 23.33, p val 4.39×10^{-37}), which have been associated with microglial changes linked to pathological insults [8], and 38 plaque-induced genes (38 of 56; OR 255.62, p val 2.4×10^{-64}) previously identified in a spatial transcriptomics characterization of the cellular response to amyloidosis [68]. These findings are therefore consistent with those of other studies using distinct approaches.

One of the most upregulated genes in this *AD-UP signature* was *GFAP*, which was also upregulated at the protein level (Additional File 2: Table S4), and we confirmed by immunofluorescence in the $App^{NL\text{-}G\text{-}F}$ model that it activates astrocytes around Aβ aggregates (Additional File 1: Fig. S6a). GFAP is an astrocyte marker, and it has been reported to accumulate in the brains of AD patients [69]. Additionally, six genes in the *AD-UP signature* (e.g., *Cd14*, *Gfap*, *Aspg*, *S1pr3*, *Ggta1*, and *Serpina3n*) were also found to be involved in astrocyte activation [70], and we found others (e.g., *Vim*) significantly upregulated in both $App^{NL\text{-}G\text{-}F}$ and 3xTg-AD mice (Additional File 1: Fig. S6b).

Overall, our *AD-UP signature* was able to recapitulate known activation pathways (microglia and astrocyte), including a significant number of known AD genetic risk factors, in response to pathological accumulation of amyloid plaques, in agreement with previous studies. Immune response to amyloid accumulation is an important part of the pathology of the disease, but the convenience or the timing for blocking or stimulating this response as a therapeutic option is still arguable [71].

On the other hand, functional enrichment analysis of the *AD-DW signature* highlighted defects on synapse transmission, synapse membrane components, neurotransmitters, or the GABA-ergic signaling system (Fig. 3c, right panel). For example, several GABA-ergic receptors such as *Gabra1*, *Gabra3*, or *Gabrb2*, as well as neuroprotective *Calb1* or *Reln* genes, were downregulated (Additional File 2: Table S4 and Fig. 3d). As these molecular defects may reflect the cognitive impairment observed in the $App^{NL\text{-}G\text{-}F}$ mice at 6 and 9 months of age, reverting some of these molecular changes could offer therapeutic opportunities [72].

Identification of proteins associated with Aβ plaques

Access to both transcriptomics and proteomics data allowed us to analyze the degree of correlation between the two datasets for proteins that were significantly up- or downregulated in the different age and AD model comparisons (Fig. 4a and Additional File 1: Fig. S7a). Of note, the changes observed at the protein level were strongly correlated with transcriptional changes in the AD models ($App^{NL\text{-}G\text{-}F}$, $App^{NL\text{-}F}$, and 3xTg-AD), indicating that many of the proteomic changes happening during Aβ pathology are triggered and regulated at the transcriptional level. This correlation was much weaker in physiological aging (3- vs. 18-mo. App^{wt}), where we observed a marked accumulation of proteins that was uncoupled from transcriptional changes. Interestingly, the proteins that accumulated in aged mice (3- vs. 18-mo. App^{wt} and $App^{NL\text{-}F}$ and 3- vs. 15- mo. 3xTg-AD) tended to have longer lifespans compared to those that accumulated in $App^{NL\text{-}G\text{-}F}$ mice, thereby suggesting that different mechanisms regulate protein homeostasis depending on the age (Fig. 4a, Additional File 1: Fig S5). We then analyzed, from a functional perspective, the proteins whose higher levels were not explained by changes at the mRNA level. We found common pathways related to pH regulation and glycogen metabolism in most aged models (i.e., 3- vs. 18-mo) App^{wt} and $App^{NL\text{-}F}$ mice, while proteins were involved in Aβ formation or metabolic processes in the most aggressive models (Fig. 4b), thereby suggesting that some of the proteins interacting with Aβ, or its precursor App may be accumulating. For instance, we found that the protein levels of Itm2c were increased in the $App^{NL\text{-}G\text{-}F}$ mice while its transcripts remained stable (Fig. 4c). Indeed, this protein has been found to co-localize with Aβ plaques in mouse and human brain samples [73, 74]. We also detected an acute increase in Ifit3 protein levels, compared to mRNA levels, in 6-mo. $App^{NL\text{-}G\text{-}F}$ mice (Fig. 4c). In a previous study, we proposed that Ifit3 might physically interact with App [75], making its aggregation in amyloid plaques plausible. IFIT family members regulate immune responses and restrict viral

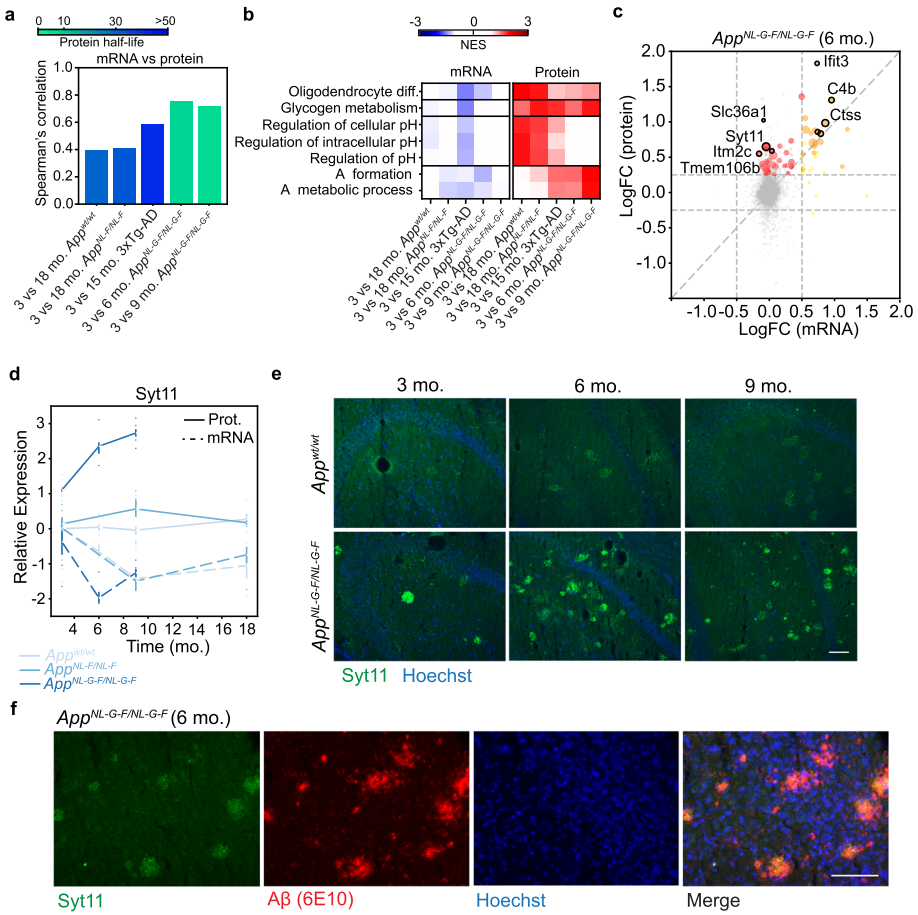

Fig. 4 Identification of Aβ-aggregated proteins through comparison of mRNA and protein levels. **a** Spearman's rank correlation of significantly altered proteins with respect to their mRNA expression in the indicated comparisons. Bar colors indicate the mean half-life of the proteins as defined by [110]. **b** Discordant upregulation of GO biological processes and Reactome pathways at protein level that is not explained by the upregulation of the same genes at mRNA level. **c** Scatter plot depicting the logarithm of the fold change (LogFC) of mRNA (*X*-axis) and protein (*Y*-axis) for the $App^{NL\text{-}G\text{-}F}$ *vs.* App^{wt} comparison at 6 mo. Proteins whose LogFC(protein) > 0.25 and their corresponding LogFC(mRNA) > 0.5 are shown in orange while those with a LogFC(protein) > 0.25 and LogFC(mRNA) < 0.5 are shown in red. Dot size is proportional to the negative logarithm of the adjusted *p* value. **d** Syt11 protein (continuous line) and mRNA (dashed line) levels at different time points relative to the App^{wt} at 3 mo. are shown for the $App^{NL\text{-}G\text{-}F}$ (strong blue), $App^{NL\text{-}F}$ (medium blue), and App^{wt} (corresponding to the $App^{NL\text{-}F}$ model; light blue) mice. $N = 4$. **e** Representative microphotographs of the hippocampus of brain sections from 3-, 6-, and 9-mo. App^{wt} (top row) or $App^{NL\text{-}G\text{-}F}$ (bottom row) mice stained with an anti-Syt11 antibody (green) and Hoechst dye (blue) ($n = 3$ for each condition). Scale bars represent 100 μm. **f** Representative micrographs of a brain section of a 6-mo. $App^{NL\text{-}G\text{-}F}$ mouse stained with an anti-Syt11 antibody (green), the anti-Aβ antibody 6E10 (red), and Hoechst dye (blue). Scale bars represent 100 μm ($n = 3$)

infections through a variety of mechanisms, including the restriction of RNA translation or binding to viral proteins [76]. Therefore, we used immunofluorescence to stain Ifit3. We observed that it formed plaque-like structures that co-localized with Aβ plaques in the brains of 6-mo. $App^{NL\text{-}G\text{-}F}$ mice but these structures were absent in App^{wt} control mice (Additional File 1: Fig. S7). Interestingly, we also identified a sharp increase in Synaptotagmin-11 (Syt11) protein levels in the $App^{NL\text{-}G\text{-}F}$ model, while its transcripts decreased (Fig. 4d). Syt11 is genetically linked to risk of Parkinson's disease [77] and it is a substrate of PRKN (encoded by *PARK2*), an E3 ubiquitin ligase that is often mutated in familial cases of Parkinson's disease [78, 79]. In mice, Syt11 deficiency in excitatory glutamatergic neurons impairs synaptic plasticity and memory [80], thereby suggesting that Syt11 dysregulation contributes to AD-associated cognitive decline. Analysis of the brain sections of 3-, 6-, and 9-mo. App^{wt} and $App^{NL\text{-}G\text{-}F}$ mice revealed Syt11 dense stains accumulating in the latter, especially at 6 and 9 months of age (Fig. 4e). Importantly, we found that Syt11 co-localized with Aβ plaques in $App^{NL\text{-}G\text{-}F}$ mice (Fig. 4f), thereby suggesting that accumulation of Syt11 in amyloid plaques contributes to the AD pathology. Moreover, a proximity-ligation assay (PLA) showed that endogenous Syt11 and App proteins

interacted in human neuron-like SH-SY5Y cells (Additional File 1: Fig. S8). Although we did not observe Syt11 dense stains in the brains of App^{NL-F} or 3xTg-AD mice at the ages tested (18 and 15 months of age, respectively), a recent proteomics analysis in the cortex of the FADx5 AD mouse model also found Ifit3 and Syt11 among the most upregulated proteins at advanced ages [81]. This finding indicates that our results could be extrapolated to other models.

Identification of approved drugs with the potential to revert AD signatures

Next, we sought to identify small molecules with the capacity to "revert" the transcriptional traits of AD mice, potentially ameliorating the disease phenotype. As a chemical space, we considered the over 800,000 bioactive compounds included in the Chemical Checker (CC) [25]. The CC provides different types of bioactivity descriptors (a.k.a. *signatures*) for each compound, including transcriptional and target profiles gathered from the major chemogenomics databases, as well as the more conventional descriptors of chemical structure. We can then use these signatures to *connect* small molecules to desired outcomes observed in phenotypic experiments such as genetic perturbation assays, as popularized in the context of transcriptomics by the Connectivity Map initiative [82]. Indeed, we proved that CC signatures could be used to identify compounds able to revert the transcriptional changes induced by AD mutations ($PSEN1^{M146V}$ and APP^{V717F}) in SH-SY5Y cells [25]. We now explored whether the capacity to prioritize compounds that revert molecular signatures could be translated to in vivo models, in which the phenotypic effects of this reversion can be measured.

We devised five distinct strategies to query the CC compound signatures based on known AD pharmacology (queries 1–3) and on the transcriptional profiles observed in our AD mouse models (queries 4–5). More specifically, we looked for compounds chemically similar to drugs clinically tested for AD [42] or with similar mechanisms of action (1), or compounds that elicited similar transcriptional responses to these drugs (2). In addition, we searched for molecules that could bind putative AD targets, as defined by OpenTargets [43] (3). Moreover, we used the CC gene expression signatures to identify compounds that trigger transcriptional changes in the opposite direction to those observed in our AD mice models (4). Likewise, we looked for shRNA experiments in the LINCS L1000 to identify knock-downs that could also revert our AD signatures, and we used them as putative AD targets to recall further candidate compounds from the CC (5). Finally, we computed blood–brain barrier penetration (BBBP) and Aβ affection scores for all the compounds, based on machine-learning models. More details on these search procedures are available in the "Methods" section. Overall, by using these five queries, we shortlisted 1% of the CC, yielding a collection of 8250 candidates (Additional File 2: Table S5). Of these, and in order to avoid issues related to compound stability and solubility in vivo, we kept only those that are commercially available and those previously tested in mice.

Among the 8250 candidate compounds, we found 125 highly ranked non-steroidal anti-inflammatory drugs (NSAIDs) targeting PTGS1 or PTGS2, which shows a very significant enrichment (p value $< 10^{-9}$) with respect to the number of similar drugs present in the CC. Moreover, we also found a significant enrichment in drugs commonly used to treat cognitive loss (i.e., acetylcholinesterase inhibitors; p value $< 10^{-6}$), which reinforces our approach. NSAIDs are one of the most widely used types of medication, being prescribed as anti-inflammatories, analgesics, and antipyretics. Although clinical trials have failed to demonstrate beneficial effects of NSAIDs in AD [83], recent articles suggest that some exert previously undescribed mechanisms of action that ameliorate AD pathology in mouse models [84, 85], thus supporting epidemiological studies reporting a potential protective effect of NSAIDs against AD [86, 87]. Thus, we selected three NSAIDs (namely etodolac, fenoprofen, and dexketoprofen) considering the scores obtained in all the described CC, and whose activity in AD had not been tested previously. Etodolac and fenoprofen are chemically similar to other NSAIDs clinically tested against AD (query 1) and they performed, in general, relatively well in all queries. Additionally, fenoprofen and dexketoprofen showed an interesting target profile (query 3), and the former also presented a high potential for reverting the transcriptional changes observed in our AD models (query 4). All three compounds presented reasonable BBBP scores (> 0.6).

The list also contained a number of approved anti-hypertensive agents, including structurally similar non-selective beta-adrenergic antagonists such as penbutolol, levobunolol, nadolol, and bupranolol. Among these, penbutolol showed a strong aggregated score for targets (query 3) and good potential for reverting transcriptional signatures (query 4) from published profiles [88] and our models. We also selected other anti-hypertensive agents with different mechanisms of action, including bendroflumethiazide, which targets sodium reabsorption, and pargyline, a MAO-A inhibitor with a relatively high score in query 3 (AD targets profile). Out of the six compounds, bendroflumethiazide showed the best reversion score for our AD signatures, ranking 31st out of the 8250 compounds sorted in the first instance, and its effects were also phenotypically similar to compounds tested in the clinics for anti-AD activity (query 2). We

also calculated a reversion score for human AD-associated signatures, extracted from [88] (see Methods). Again, bendroflumethiazide showed an extremely high score (3.82), being the 37th best score among the 8250 preselected compounds.

We assessed the effectiveness of the selected compounds on the $App^{NL\text{-}G\text{-}F}$ model, since it shows cognitive deficits at early stages. We treated 5-mo. mice with the different drugs for 4 weeks and, during the characterization of the models, we evaluated the effects of the drugs in the NOR test. We then collected hippocampi samples for further molecular analyses (Fig. 5a). As we had already observed, $App^{NL\text{-}G\text{-}F}$ mice treated with vehicle performed worse (48.6 ± 12.5% for vehicle 1 and 53.5 ± 15.7% for vehicle 2) than age-matched App^{wt} mice in the NOR test (60.1 ± 10.7% for vehicle 1 and 58.0 ± 10.5% for vehicle 2) (Fig. 5b). On average, $App^{NL\text{-}G\text{-}F}$ mice treated with bendroflumethiazide (62.4 ± 18.4%), dexketoprofen (55.7 ± 6.1%), etodolac (57.5 ± 23.3%), or penbutolol (68.1 ± 15.5%) performed better than the corresponding control mice treated with vehicle. However, we did not appreciate any cognitive improvement in the mice treated with fenoprofen (47.3 ± 17.0%) or pargyline (49.6 ± 4.7%). Overall, four out of the six treatments assayed yielded NOR results comparable to those of wild-type animals, thereby pointing to the potential rescuing of the cognition impairment associated with *App* mutations.

In view of these results, we analyzed the gene expression changes in the hippocampi of $App^{NL\text{-}G\text{-}F}$ mice treated with the compounds that showed a beneficial effect in the NOR test (bendroflumethiazide, dexketoprofen, etodolac, and penbutolol) and the corresponding controls (vehicle-treated $App^{NL\text{-}G\text{-}F}$ and App^{wt} mice; Additional File 2: Table S6). As expected, analysis of App^{wt} and $App^{NL\text{-}G\text{-}F}$ controls showed similar transcriptional signatures compared with our previous characterization of the model (data not shown). Indeed, the four compounds significantly downregulated the expression of genes upregulated in the AD signature, thus being able to revert these characteristic transcriptional changes related to Aβ pathology. Of the four compounds, bendroflumethiazide and penbutolol showed the strongest effects (blue lines, Fig. 5c). Functional enrichment analysis of these reverted genes showed significant association with phagocytosis and activation of the immune response pathways (Additional File 1: Fig. S9a), which is coherent with the strong component of immune system activation found in the signatures of the AD mouse models and the fact that these signatures were used to prioritize the selection of potential drugs. Genes such as *Cx3cr1* or *Tyrobp*, previously identified as part of the *AD-UP signature*, were partially downregulated in bendroflumethiazide-treated $App^{NL\text{-}G\text{-}F}$ mice compared with vehicle-treated mice (Fig. 5d and Fig. 5e), suggesting that this drug may inhibit microglia activation. Bendroflumethiazide is an anti-hypertensive drug that exerts its effect by inhibiting sodium reabsorption at the beginning of the distal convoluted tubule. Although Na^+ influx has been linked to activation of the inflammasome [89], we could not find previous reports detecting or suggesting a potential anti-inflammatory role.

Although all four treatments reverted the tendency of upregulated genes in AD signatures, only penbutolol treatment also induced the reversion of a significant proportion of the *AD-DW signature* in $App^{NL\text{-}G\text{-}F}$ mice (Fig. 5c; red lines). Penbutolol prevented the Aβ-associated downregulation of genes such as the gamma-aminobutyric acid (GABA) receptor *Gabrb2* or the glutamate receptor *Grm8*, keeping their expression at physiological levels (Fig. 5d, e).

Next, we used immunofluorescence to quantify Aβ accumulation in the brains of treated $App^{NL\text{-}G\text{-}F}$ mice. The percentage of Aβ-positive area in the DG-CA1 hippocampal regions of $App^{NL\text{-}G\text{-}F}$ mice treated with penbutolol (5.1 ± 1.6%) was reduced compared with mice treated with the corresponding vehicle (6.3 ± 1.8%; Additional File 1: Fig. S10a). As expected, App^{wt} animals did not show Aβ staining. Other treatments did not seem to have an effect on Aβ accumulation when compared to the corresponding vehicles (data not shown). To further validate the effect of penbutolol, we treated neuron-like SH-SY5Y cells, which are known to recapitulate phenotypes related to neurodegenerative disorders [90]. Indeed, we observed that penbutolol inhibited the secretion of $A\beta_{40}$ (47.5 ± 15.5% at 25 μM) in a dose-dependent manner, while a minor effect was observed for $A\beta_{42}$ secretion (78.8 ± 14.2% at 25 μM), without any observed toxicity (Additional File 1: Fig. S10b). Additionally, we tested the compounds in genetically modified SH-SY5Y cells harboring the familial AD mutation $PSEN1^{M146V/M146V}$ [25], which increases $A\beta_{40}$ (1.6 ± 0.3 fold) and $A\beta_{42}$ (3.4 ± 0.2 fold) secretion (Additional File 1: Fig. S10b). Like in wild-type cells, penbutolol inhibited the secretion of $A\beta_{40}$ (67.2 ± 6.3% of DMSO control at 25 μM) in $PSEN1^{M146V/M146V}$ cells (Additional File 1: Fig. S10b). Finally, we tested the effect of these compounds in the 7PA2 cell line, a well-established model for screening compounds targeting Aβ production [91]. In accordance with the in vivo observation, penbutolol inhibited $A\beta_{40}$ (16.1 ± 10.0% at 25 μM) and $A\beta_{42}$ (30.9 ± 24.0% at 25 μM) at relatively low concentrations, showing a dose-dependent response. Fenoprofen showed a similar trend, although the inhibition of $A\beta_{40}$ was milder (53.3 ± 4.7% at 500 μM), while the remaining four compounds did not exhibit any significant effect (Additional File 1: Fig. S10c).

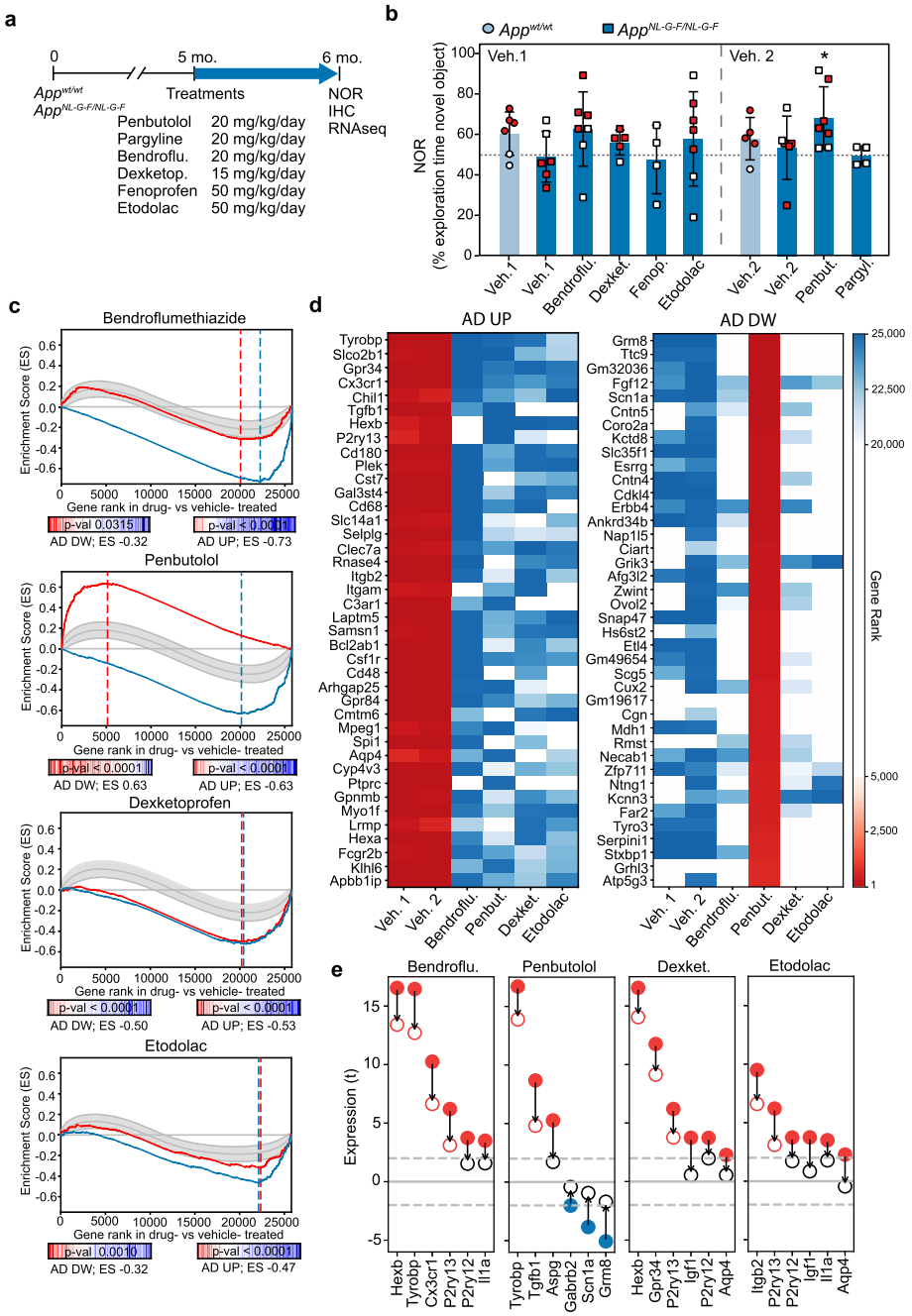

Fig. 5 (See legend on next page.)

(See figure on previous page.)
Fig. 5 In vivo reversion of AD signatures. **a** Scheme of drug treatments and evaluation **b** Novel object recognition (NOR) test of 6-month-old animals. App^{wt} (circles; light blue) and App^{NL-F} (squares; dark blue) mice were treated for 4 weeks with the indicated drugs. Mean ± SD of the % of time exploring the novel object is shown (n = 4–7). One-sample t-test vs. a hypothetical value of 50 (* p value < 0.05). Red points indicate the animals selected for RNAseq analysis. **c** Signature reversion. In the X-axis, genes are ranked by their differential expression in the comparison of drug- vs. vehicle-treated App^{NL-G-F} mice. The Y-axis represents the running Enrichment Score (ES) performed for the *AD signatures* (*AD-UP*, blue; *AD-DW*, red) that were reverted upon treatment. Dashed vertical lines indicate the point at which the ES reaches its maximum deviation from zero, defining the leading-edge subset of genes that contribute the most to the enrichment result. The observed ES is compared to a null distribution of 10,000 randomized signatures of the same size (95% CI shown as a shaded gray area). For example, *AD-DW signature* genes (red line) tend to be ranked among the 5000 most upregulated genes in response to penbutolol treatment (second panel), with an ES of 0.63, which is significantly higher than that of random signatures of the same size (p value < 0.0001). This is interpreted as a significant signature reversion. RNAseq data were obtained from n = 4 mice per condition. **d** Heatmaps showing the *reversion rank* of the top-40 genes belonging to the leading-edge of the *AD-UP signature* (blue; left panel) and *AD-DW signature* (red; right panel) in two or more treatments, sorted by the average row value. Data obtained from n = 4 mice per condition. **e** Leading-edge genes of the *AD-UP* and *AD-DW signatures* reverted by the different treatments. We show a few genes in the AD signatures that are up- (red) or down- (blue) regulated (t-score) in the vehicle-treated App^{NL-G-F} mice compared with vehicle-treated App^{wt} animals (bold dots) or in the drug-treated App^{NL-G-F} mice compared with vehicle-treated App^{wt} animals (empty dots). RNAseq data were obtained from n = 4 mice per condition

We had previously identified astrocytosis as an important component of the AD-associated molecular changes in our mouse models (Additional File 1: Fig. S6) and, interestingly, *Gfap* was one of the genes whose expression was partially downregulated in response to penbutolol (Additional File 1: Fig. S10d). Moreover, penbutolol was able to significantly revert the previously defined astrocytic signature (Additional File 1: Fig. S10d). Also, the percentage of GFAP immunofluorescence positive area was slightly reduced in the brain sections of App^{NL-G-F} mice treated with penbutolol (12.3 ± 3.7%) when compared with vehicle-treated mice (14.3 ± 4.3%; Additional File 1: Fig. S10e) and, as expected, in both cases we observed more GFAP staining than in the corresponding age-matched App^{wt} mice (8.8 ± 2.4% for vehicle 2).

Overall, our results consistently suggest that penbutolol inhibits Aβ production, accompanied by a reversion of the AD signature, both ameliorating inflammation, astrocytosis, and loss of synaptic genes. Although the phenotype reversion is mild, optimized regime treatments (e.g., longer treatment, earlier treatment or improved delivery) might improve the results.

Discussion

In this manuscript, we present the complete characterization of three murine models at different stages representative of Alzheimer´s disease (AD) (i.e., onset, progression and advanced). To identify genotype-to-phenotype relationships, we combined the cognitive assessment of these mice with histological analyses and a full transcriptional and protein quantification profiling from the hippocampus. As expected, we confirmed previously reported findings in these AD models, such as the age at which cognitive decline starts and when the presence of Aβ plaques becomes detectable [49, 50]. We also confirmed that the most aggressive model (e.g., App^{NL-G-F}) shows more changes in genes/proteins compared to healthy mice, although a significant number of dysregulated genes/proteins are shared between the three models, and that most of these changes take place at disease onset. Our comparison between AD progression and healthy aging revealed certain commonalities, such as the upregulation of microglial and inflammation markers. However, the observation that 18-mo. healthy mice do not show any cognitive decline indicates that, although accelerated aging occurs in AD models, there are other factors specifically associated with Aβ pathology. Comparison of transcriptional and quantitative protein profiles from the same mice revealed a clear correlation between mRNA and protein levels of the dysregulated genes. This observation thus supports the notion that most changes are indeed a consequence of expression changes. Interestingly, this correlation was much weaker in physiological aging, where the observed accumulation of proteins was decoupled from transcriptional changes. We also found a few proteins whose abundance increased with AD progression, while the corresponding transcript levels remained stable. These were potential cases of protein accumulation in disease conditions, and we showed that at least two of these proteins, namely Ifit3 and Syt11, co-localize with Aβ plaques in the brain. Moreover, we also observed that these proteins tend to have a shorter lifespan than those found to accumulate in healthy old mice, suggesting different mechanisms of homeostasis regulation. Progressive decoupling of mRNA and protein expression profiles associated with aging has been reported in yeast [92] and human and rhesus macaque brains [93]. Excluding technical issues, it is believed that discrepancies between protein and mRNA levels are mainly determined by translation and protein degradation [94, 95], although it has been suggested a major influence of protein turnover [96]. Since many proteins have been found co-localizing with Aβ in plaques in neurodegenetarive diseases [97], it is a plausible hypothesis that

some of the decoupled proteins are localized in Aβ plaques, altering their normal turnover. Finally, we took advantage of the transcriptional profiles of two knock-in mice (e.g., App^{NL-F} and App^{NL-G-F}) to derive specific Aβ-related AD signatures, which showed a clear mobilization of microglia and astrocytes, thus reflecting the activation of the brain immune system in response to Aβ accumulation. Additionally, these effects were accompanied by the downregulation of synapse transmission processes. Interestingly, most of the functional processes associated with the characteristic AD signatures were also dysregulated in the 3xTg-AD model, thus supporting their general validity beyond AD models harboring single *App* mutations.

Despite the many efforts and a great number of clinical trials, only 5 drugs have been approved for the treatment of AD (i.e., 4 cholinesterase inhibitors and a N-methyl-D-aspartate (NMDA) antagonist with neuroprotective properties), and these are mostly symptomatic drugs that do not tackle the etiology of the disease [17]. A lack of appropriate biomarkers, incomplete preclinical data, and difficulties to start treatments at early stages of the disease may explain these failures [19, 20]. Additionally, given the robustness of biological systems, it is also clear that the inhibition of a single target (i.e., the β-secretase) is not enough to alter the progression of the disease, and we need to look beyond the "one disease, one target, one drug" paradigm. In an attempt to tackle AD from a global perspective, we profited from our recently derived compound bioactivity descriptors to find small molecules able to neutralize the changes induced by the disease [25]. Of the ~1 M compounds, we selected six drugs, including three non-steroidal anti-inflammatory drugs (NSAIDs) and three anti-hypertensives with very different reported mechanisms of action, that showed a good potential to revert the AD signatures in silico. Note that none of the selected drugs have been previously tested against AD in clinical trials or pre-clinical mouse models. After a 4-week treatment, we demonstrated that four of the six drugs, two NSAIDs (dexketoprofen and etodolac) and two anti-hypertensives (penbutolol and bendroflumethiazide), reduced the cognitive impairment in AD mice. We also demonstrated that all four compounds partially reverted the expression levels of those genes upregulated in our AD signatures, although only penbutolol was able to significantly restore the global expression levels of genes repressed in AD. Reassuringly, only the hippocampi of mice treated with this antagonist of β-adrenergic receptors showed a reduction of Aβ plaques and a clear dose-dependent inhibition of $A\beta_{40}$ and $A\beta_{42}$ production in vitro. Thus, the beneficial effects on cognition observed with bendroflumethiazide, dexketoprofen, and etodolac could be more associated with the reversion of immune system activation signature to a homeostatic state rather than a direct effect on Aβ clearance.

Epidemiological studies identified NSAIDs and anti-hypertensives as protective agents against AD [86, 87], with the potential to target the Aβ processing pathway [98]. Unfortunately, randomized clinical trials did not show positive effects for a number of NSAIDs (e.g., R-flurbiprofen, indomethacin, rofecoxib, naproxen, or celecoxib), and some adverse events were reported associated with their prolonged use (e.g., cardiovascular risk [99]). There is an ongoing discussion on the possibility that clinical trials testing NSAIDs might not have been fully comprehensive, and dosage, CNS-permeability, or different patient-group selection could have had an impact on the trial outcome [100]. Thus, targeting inflammation as a contributor to cognitive loss remains a viable goal [101–103], but we are still lacking the right biomarkers to address the effect of NSAIDs on AD-mediated neuroinflammation. On the positive side, it has been reported that a 3-month treatment of a mouse model of AD with ibuprofen prevents memory impairment, although without any perceivable change in Aβ accumulation or inflammation [85]. Recent studies also showed that fenamate NSAID has the potential to block AD pathology in animal models through COX-2-independent inhibition of the NLRP3 inflammasome [84]. On the other hand, as hypertension in midlife is a risk factor for dementia [104], anti-hypertensive drugs have been proposed as potential preventive treatments for AD [105]. Indeed, compounds targeting noradrenergic signaling, such as prazosin [106] and carvedilol [107], have shown beneficial effects on AD mouse models by alternative mechanisms, including the blockade of Aβ production and neuronal protection, although an increased risk of Parkinson's disease has been associated to the use of nonselective β-adrenergic antagonists [108, 109].

Given the strong linkage found between the inflammatory signature and AD progression, it is tempting to attribute the beneficial effects that we observed with dexketoprofen and etodolac to the anti-inflammatory role of NSAIDs, especially in view of the reversion of the AD-UP, highly influenced by inflammatory response, which have been linked to microglial response. Additionally, recent studies suggest that PTGS2 (COX2) may play a role in several signaling pathways activated in neurons, affecting neurotransmission and neuronal plasticity [85]; therefore, more than one functional process may be contributing to the overall mechanism of action of the drugs. Following a similar reasoning, we may speculate that bendroflumethiazide may have an anti-inflammatory role, in view of the *AD-UP signature* reversion of known microglial genes. Although

bendroflumethiazide showed the best predicted reversion score for our AD signatures in our virtual drug screening, we have not been able to find previous reports indicating a role of bendroflumethiazide in inflammation, so further investigation will be required to address the mechanism of action of this drug in cellular models of microglia, for example. Finally, penbutolol did show a mild effect on Aβ accumulation, corroborated by our in vitro models. Compounds targeting noradrenergic signaling, such as prazosin [106] and carvedilol [107], have shown beneficial effects on AD mouse models by alternative mechanisms, including the blockade of Aβ production and neuronal protection. Given the modest effect of penbutolol on Aβ accumulation, we hypothesize that it could be acting through several mechanisms, including the reversion of the astrocytic signature through the downregulation of Gfap. We cannot discriminate, however, whether this effect on astrocytosis is the consequence of the decrease in Aβ accumulation, and further research will be required to address the specific effect of this drug in different types of cells (microglia, neurons, astrocytes, etc.).

Conclusions

The characterization of three AD mouse models at different disease stages has provided an unprecedented view of AD pathology and how this differs from physiological ageing. Moreover, our computational strategy to chemically revert AD signatures has shown that, despite the inconclusive and contradictory results reported, NSAID and anti-hypertensive drugs may still have an opportunity as anti-AD agents.

Supplementary Information

The online version contains supplementary material available at https://doi.org/10.1186/s13073-021-00983-y.

Additional file 1. File including all supplementary figures cited in the text (FigS1-S10), the Table S7 and legends to all the supplementary tables (Table S1-S6) included in the Additional File 2.

Additional file 2. Compressed file including the supplementary tables (Table S1-S6).

Acknowledgements

We would like to thank Prof. E Wanker and his team at MDC-Berlin for helpful discussions. The authors acknowledge the support of the IRB Barcelona Proteomics and Biostatistics Units.

Authors' contributions

EP, SB, LM, MD-F, and PA designed the study. EP, SB, and VA performed all the in vivo and in vitro studies. EP, LM, and TJ-B analyzed the results, with the help of AB-LI and CS-OA to process and analyze the transcriptomics and proteomics data. MD-F implemented the computational strategy to find potential chemical modulators of AD. MG and EdO performed quantitative proteomics experiments. TCS and TS provided the knock-in mouse models. All the authors discussed and interpreted the results. EP, LM, MD-F, and PA wrote the manuscript, which has been approved by all the authors. All the authors read and approved the final manuscript.

Funding

PA acknowledges the support of the Generalitat de Catalunya (RIS3CAT Emergents CECH: 001-P-001682 and VEIS: 001-P-001647), the Spanish Ministerio de Economía y Competitividad (BIO2016-77038-R), and the European Research Council (SysPharmAD: 614944).

Availability of data and materials

All the mRNAseq data have been deposited in the Gene Expression Omnibus (GEO [52]; database with the identifier GSE168431 (https://www.ncbi.nlm.nih.gov/geo/query/acc.cgi?acc = GSE168431). The mass spectrometry proteomics data have been deposited to the ProteomeXchange Consortium via the PRIDE [38] partner repository with the dataset identifier PXD024538 (https://www.ebi.ac.uk/pride/archive/projects/PXD024538).

Declarations

Ethics approval and consent to participate

All the animal experiments have been performed following the Ethics Committee rules of the Institute following the current European legislation (Council Directive 86/609/EEC; Law 5/1995/GC; Order 214/1997/GC; Law 1201/2005/SG) and all the protocols have been authorized by the Direcció General del Medi Ambient i Biodiversitat (Calatalan Government) n° DAM:5880 (authorization numbers 8478, 8527 and 10382).

Consent for publication

Not applicable.

Competing interests

The authors declare that they have no competing interests.

Author details

[1]Joint IRB-BSC-CRG Programme in Computational Biology, Institute for Research in Biomedicine (IRB Barcelona), The Barcelona Institute of Science and Technology, Barcelona, Catalonia, Spain. [2]Laboratory for Proteolytic Neuroscience, RIKEN Center for Brain Science, Wako, Saitama 351-0198, Japan. [3]Department of Neurocognitive Science, Institute of Brain Science, Nagoya City University Graduate School of Medical Sciences, Nagoya, Japan. [4]Biostatistics and Bioinformatics Unit, Institute for Research in Biomedicine (IRB Barcelona), The Barcelona Institute of Science and Technology, Barcelona, Catalonia, Spain. [5]Proteomics Unit, Institute for Research in Biomedicine (IRB Barcelona), The Barcelona Institute of Science and Technology, Barcelona, Catalonia, Spain. [6]Proteomics Platform, Barcelona Science Park, Barcelona, Catalonia, Spain. [7]Institució Catalana de Recerca i Estudis Avançats (ICREA), Barcelona, Catalonia, Spain.

Received: 16 April 2021 Accepted: 29 September 2021
Published online: 26 October 2021

References

1. Goedert M, Spillantini MG. A century of Alzheimer's disease. *Science*. 2006; 314(5800):777–81. https://doi.org/10.1126/science.1132814.
2. Tanzi RE. The genetics of Alzheimer disease. *Cold Spring Harb Perspect Med*. 2012;2(10). https://doi.org/10.1101/cshperspect.a006296.
3. Selkoe DJ, Hardy J. The amyloid hypothesis of Alzheimer's disease at 25 years. *EMBO Mol Med*. 2016;8(6):595–608. https://doi.org/10.15252/emmm.201606210.
4. Ashe KH, Zahs KR. Probing the biology of Alzheimer's disease in mice. *Neuron*. 2010;66(5):631–45. https://doi.org/10.1016/j.neuron.2010.04.031.
5. LaFerla FM, Green KN. Animal models of Alzheimer disease. *Cold Spring Harb Perspect Med*. 2012;**2**(11). https://doi.org/10.1101/cshperspect.a006320.
6. Castillo E, Leon J, Mazzei G, Abolhassani N, Haruyama N, Saito T, et al. Comparative profiling of cortical gene expression in Alzheimer's disease patients and mouse models demonstrates a link between amyloidosis and neuroinflammation. *Sci Rep*. 2017;7:17762.
7. Matarin M, Salih DA, Yasvoina M, Cummings DM, Guelfi S, Liu W, et al. A genome-wide gene-expression analysis and database in transgenic mice during development of amyloid or tau pathology. *Cell Rep*. 2015;10(4):633–44. https://doi.org/10.1016/j.celrep.2014.12.041.
8. Keren-Shaul H, Spinrad A, Weiner A, Matcovitch-Natan O, Dvir-Szternfeld R, Ulland TK, et al. A unique microglia type associated with restricting

development of Alzheimer disease. *Cell*. 2017;169(7):1276–90 e1217. https://doi.org/10.1016/j.cell.2017.05.018.
9. Mathys H, Adaikkan C, Gao F, Young JZ, Manet E, Hemberg M, et al. Temporal tracking of microglia activation in neurodegeneration at single-cell resolution. *Cell Rep*. 2017;21(2):366–80. https://doi.org/10.1016/j.celrep.2017.09.039.
10. Kim DK, Han D, Park J, Choi H, Park JC, Cha MY, et al. Deep proteome profiling of the hippocampus in the 5XFAD mouse model reveals biological process alterations and a novel biomarker of Alzheimer's disease. *Exp Mol Med*. 2019;51:136.
11. Kim DK, Park J, Han D, Yang J, Kim A, Woo J, et al. Molecular and functional signatures in a novel Alzheimer disease mouse model assessed by quantitative proteomics. *Mol Neurodegener*. 2018;13(1):2. https://doi.org/10.1186/s13024-017-0234-4.
12. Lv J, Ma S, Zhang X, Zheng L, Ma Y, Zhao X, et al. Quantitative proteomics reveals that PEA15 regulates astroglial Abeta phagocytosis in an Alzheimer's disease mouse model. *J Proteomics*. 2014;110:45–58.
13. Martin B, Brenneman R, Becker KG, Gucek M, Cole RN, Maudsley S. iTRAQ analysis of complex proteome alterations in 3xTgAD Alzheimer's mice: understanding the interface between physiology and disease. *PLoS One*. 2008;3(7):e2750. https://doi.org/10.1371/journal.pone.0002750.
14. Savas JN, Wang YZ, DeNardo LA, Martinez-Bartolome S, McClatchy DB, Hark TJ, et al. Amyloid accumulation drives proteome-wide alterations in mouse models of Alzheimer's disease-like pathology. *Cell Rep*. 2017;21(9):2614–27. https://doi.org/10.1016/j.celrep.2017.11.009.
15. Ori A, Toyama BH, Harris MS, Bock T, Iskar M, Bork P, et al. Integrated transcriptome and proteome analyses reveal organ-specific proteome deterioration in old rats. *Cell Syst*. 2015;1(3):224–37. https://doi.org/10.1016/j.cels.2015.08.012.
16. Citron M. Alzheimer's disease: strategies for disease modification. *Nat Rev Drug Discov*. 2010;9(5):387–98. https://doi.org/10.1038/nrd2896.
17. Mangialasche F, Solomon A, Winblad B, Mecocci P, Kivipelto M. Alzheimer's disease: clinical trials and drug development. *Lancet Neurol*. 2010;9(7):702–16. https://doi.org/10.1016/S1474-4422(10)70119-8.
18. Selkoe DJ. Resolving controversies on the path to Alzheimer's therapeutics. *Nat Med*. 2011;17:1060–5.
19. De Strooper B. Lessons from a failed gamma-secretase Alzheimer trial. *Cell*. 2014;159(4):721–6. https://doi.org/10.1016/j.cell.2014.10.016.
20. Karran E, Hardy J. A critique of the drug discovery and phase 3 clinical programs targeting the amyloid hypothesis for Alzheimer disease. *Ann Neurol*. 2014;76(2):185–205. https://doi.org/10.1002/ana.24188.
21. Iorio F, Rittman T, Ge H, Menden M, Saez-Rodriguez J. Transcriptional data: a new gateway to drug repositioning. *Drug Discov Today*. 2013;18(7-8):350–7. https://doi.org/10.1016/j.drudis.2012.07.014.
22. Liu J, Lee J, Salazar Hernandez MA, Mazitschek R, Ozcan U. Treatment of obesity with celastrol. *Cell*. 2015;161(5):999–1011. https://doi.org/10.1016/j.cell.2015.05.011.
23. Brum AM, van de Peppel J, van der Leije CS, Schreuders-Koedam M, Eijken M, van der Eerden BC, et al. Connectivity Map-based discovery of parbendazole reveals targetable human osteogenic pathway. *Proc Natl Acad Sci U S A*. 2015;112(41):12711–6. https://doi.org/10.1073/pnas.1501597112.
24. Janssens GE, Lin XX, Millan-Arino L, Kavsek A, Sen I, Seinstra RI, et al. Transcriptomics-based screening identifies pharmacological inhibition of Hsp90 as a means to defer aging. *Cell Rep*. 2019;27:467–80 e466.
25. Duran-Frigola M, Pauls E, Guitart-Pla O, Bertoni M, Alcalde V, Amat D, et al. Extending the small molecule similarity principle to all levels of biology. *Nat Biotechnol*. 2020;38(9):1087–96.
26. Das S, Au E, Krazit ST, Pandey KN. Targeted disruption of guanylyl cyclase-A/natriuretic peptide receptor-A gene provokes renal fibrosis and remodeling in null mutant mice: role of proinflammatory cytokines. *Endocrinology*. 2010;151(12):5841–50. https://doi.org/10.1210/en.2010-0655.
27. Miranda HF, Puig MM, Dursteler C, Prieto JC, Pinardi G. Dexketoprofen-induced antinociception in animal models of acute pain: synergy with morphine and paracetamol. *Neuropharmacology*. 2007;52(2):291–6. https://doi.org/10.1016/j.neuropharm.2006.07.025.
28. Montero-Melendez T, Forfar RA, Cook JM, Jerman JC, Taylor DL, Perretti M. Old drugs with new skills: fenoprofen as an allosteric enhancer at melanocortin receptor 3. *Cell Mol Life Sci*. 2017;74(7):1335–45. https://doi.org/10.1007/s00018-016-2419-3.
29. Tanaka K, Yamamoto Y, Tsujimoto S, Uozumi N, Kita Y, Yoshida A, et al. The cyclooxygenase-2 selective inhibitor, etodolac, but not aspirin reduces neovascularization in a murine ischemic hind limb model. *Eur J Pharmacol*. 2010;627(1-3):223–8. https://doi.org/10.1016/j.ejphar.2009.10.058.
30. Trevisan da Rocha J, Mozzaquatro Gai B, Pinton S, Bazanella Sampaio T, Nogueira CW, Zeni G. Effects of diphenyl diselenide on depressive-like behavior in ovariectomized mice submitted to subchronic stress: involvement of the serotonergic system. *Psychopharmacology (Berl)*. 2012;222(4):709–19. https://doi.org/10.1007/s00213-012-2675-3.
31. Zhan DY, Morimoto S, Du CK, Wang YY, Lu QW, Tanaka A, et al. Therapeutic effect of {beta}-adrenoceptor blockers using a mouse model of dilated cardiomyopathy with a troponin mutation. *Cardiovasc Res*. 2009;84(1):64–71. https://doi.org/10.1093/cvr/cvp168.
32. Leger M, Quiedeville A, Bouet V, Haelewyn B, Boulouard M, Schumann-Bard P, et al. Object recognition test in mice. *Nat Protoc*. 2013;8(12):2531–7. https://doi.org/10.1038/nprot.2013.155.
33. Carroll JC, Rosario ER, Kreimer S, Villamagna A, Gentzschein E, Stanczyk FZ, et al. Sex differences in beta-amyloid accumulation in 3xTg-AD mice: role of neonatal sex steroid hormone exposure. *Brain Res*. 2010;1366:233–45. https://doi.org/10.1016/j.brainres.2010.10.009.
34. Harrow J, Denoeud F, Frankish A, Reymond A, Chen CK, Chrast J, et al. GENCODE: producing a reference annotation for ENCODE. *Genome Biol*. 2006;7(Suppl 1:S4):1–9.
35. Rossell D, Stephan-Otto Attolini C, Kroiss M, Stocker A. Quantifying alternative splicing from paired-end RNA-sequencing data. *Ann Appl Stat*. 2014;8(1):309–30. https://doi.org/10.1214/13-aoas687.
36. Smyth GK. Linear models and empirical Bayes methods for assessing differential expression in microarray experiments. *Stat Appl Genet Mol Biol*. 2004;3:Article3.
37. Subramanian A, Tamayo P, Mootha VK, Mukherjee S, Ebert BL, Gillette MA, et al. Gene set enrichment analysis: a knowledge-based approach for interpreting genome-wide expression profiles. *Proc Natl Acad Sci U S A*. 2005;102(43):15545–50. https://doi.org/10.1073/pnas.0506580102.
38. Perez-Riverol Y, Csordas A, Bai J, Bernal-Llinares M, Hewapathirana S, Kundu DJ, et al. The PRIDE database and related tools and resources in 2019: improving support for quantification data. *Nucleic Acids Res*. 2019;47:D442–50.
39. Love MI, Huber W, Anders S. Moderated estimation of fold change and dispersion for RNA-seq data with DESeq2. *Genome Biol*. 2014;15(12):550. https://doi.org/10.1186/s13059-014-0550-8.
40. Bates D, Mächler M, Bolker B, Walker S. Fitting linear mixed-effects models using lme4. *J Stat Soft*. 2015;67(1):48. https://doi.org/10.18637/jss.v067.i01.
41. Hothorn T, Bretz F, Westfall P. Simultaneous inference in general parametric models. *Biom J*. 2008;50:346–63.
42. Kinoshita J, Clark T. Alzforum. *Methods Mol Biol*. 2007;401:365–81. https://doi.org/10.1007/978-1-59745-520-6_19.
43. Ochoa D, Hercules A, Carmona M, Suveges D, Gonzalez-Uriarte A, Malangone C, et al. Open Targets Platform: supporting systematic drug-target identification and prioritisation. *Nucleic Acids Res*. 2021;49(D1):D1302–10. https://doi.org/10.1093/nar/gkaa1027.
44. Subramanian A, Narayan R, Corsello SM, Peck DD, Natoli TE, Lu X, et al. A next generation connectivity map: L1000 platform and the first 1,000,000 profiles. *Cell*. 2017;171:1437–1452.e1417.
45. Wu Z, Ramsundar B, Feinberg EN, Gomes J, Geniesse C, Pappu AS, et al. MoleculeNet: a benchmark for molecular machine learning. *Chem Sci*. 2018;9(2):513–30. https://doi.org/10.1039/C7SC02664A.
46. Kondo T, Imamura K, Funayama M, Tsukita K, Miyake M, Ohta A, et al. iPSC-based compound screening and in vitro trials identify a synergistic anti-amyloid beta combination for Alzheimer's disease. *Cell Rep*. 2017;21(8):2304–12. https://doi.org/10.1016/j.celrep.2017.10.109.
47. Bertoni M, Duran-Frigola M, Badia-i-Mompel P, Orozco-Ruiz M, Guitart-Pla O, Aloy P. Bioactivity descriptors for uncharacteized compounds. *bioRxiv*. 2020.
48. Sasaguri H, Nilsson P, Hashimoto S, Nagata K, Saito T, De Strooper B, et al. APP mouse models for Alzheimer's disease preclinical studies. *EMBO J*. 2017;36(17):2473–87. https://doi.org/10.15252/embj.201797397.
49. Saito T, Matsuba Y, Mihira N, Takano J, Nilsson P, Itohara S, et al. Single App knock-in mouse models of Alzheimer's disease. *Nat Neurosci*. 2014;17(5):661–3. https://doi.org/10.1038/nn.3697.
50. Oddo S, Caccamo A, Shepherd JD, Murphy MP, Golde TE, Kayed R, et al. Triple-transgenic model of Alzheimer's disease with plaques and tangles: intracellular Abeta and synaptic dysfunction. *Neuron*. 2003;39(3):409–21. https://doi.org/10.1016/S0896-6273(03)00434-3.

51. Ross PL, Huang YN, Marchese JN, Williamson B, Parker K, Hattan S, et al. Multiplexed protein quantitation in Saccharomyces cerevisiae using amine-reactive isobaric tagging reagents. *Mol Cell Proteomics*. 2004;3(12):1154–69. https://doi.org/10.1074/mcp.M400129-MCP200.
52. Barrett T, Wilhite SE, Ledoux P, Evangelista C, Kim IF, Tomashevsky M, et al. NCBI GEO: archive for functional genomics data sets-update. *Nucleic Acids Res*. 2013;41(Database issue):D991–5. https://doi.org/10.1093/nar/gks1193.
53. Marlatt MW, Potter MC, Bayer TA, van Praag H, Lucassen PJ. Prolonged running, not fluoxetine treatment, increases neurogenesis, but does not alter neuropathology, in the 3xTg mouse model of Alzheimer's disease. *Curr Top Behav Neurosci*. 2013;15:313–40.
54. Hammond TR, Dufort C, Dissing-Olesen L, Giera S, Young A, Wysoker A, et al. Single-Cell RNA sequencing of microglia throughout the mouse lifespan and in the injured brain reveals complex cell-state changes. *Immunity*. 2019;50(1):253–71 e256. https://doi.org/10.1016/j.immuni.2018.11.004.
55. Ximerakis M, Lipnick SL, Innes BT, Simmons SK, Adiconis X, Dionne D, et al. Single-cell transcriptomic profiling of the aging mouse brain. *Nat Neurosci*. 2019;22(10):1696–708. https://doi.org/10.1038/s41593-019-0491-3.
56. Lopez-Otin C, Blasco MA, Partridge L, Serrano M, Kroemer G. The hallmarks of aging. *Cell*. 2013;153(6):1194–217. https://doi.org/10.1016/j.cell.2013.05.039.
57. Marciniak E, Faivre E, Dutar P, Alves Pires C, Demeyer D, Caillierez R, et al. The chemokine MIP-1alpha/CCL3 impairs mouse hippocampal synaptic transmission, plasticity and memory. *Sci Rep*. 2015;5(1):15862. https://doi.org/10.1038/srep15862.
58. Llorens F, Hermann P, Villar-Pique A, Diaz-Lucena D, Nagga K, Hansson O, et al. Cerebrospinal fluid lipocalin 2 as a novel biomarker for the differential diagnosis of vascular dementia. *Nat Commun*. 2020;11(1):619. https://doi.org/10.1038/s41467-020-14373-2.
59. Patra K, Soosaipillai A, Sando SB, Lauridsen C, Berge G, Moller I, et al. Assessment of kallikrein 6 as a cross-sectional and longitudinal biomarker for Alzheimer's disease. *Alzheimers Res Ther*. 2018;10(1):9. https://doi.org/10.1186/s13195-018-0336-4.
60. Abraham CR, Selkoe DJ, Potter H. Immunochemical identification of the serine protease inhibitor alpha 1-antichymotrypsin in the brain amyloid deposits of Alzheimer's disease. *Cell*. 1988;52(4):487–501. https://doi.org/10.1016/0092-8674(88)90462-X.
61. Vanni S, Moda F, Zattoni M, Bistaffa E, De Cecco E, Rossi M, et al. Differential overexpression of SERPINA3 in human prion diseases. *Sci Rep*. 2017;7(1):15637. https://doi.org/10.1038/s41598-017-15778-8.
62. Castanho I, Murray TK, Hannon E, Jeffries A, Walker E, Laing E, et al. Transcriptional signatures of tau and amyloid neuropathology. *Cell Rep*. 2020;30(6):2040–54 e2045. https://doi.org/10.1016/j.celrep.2020.01.063.
63. Giannopoulos PF, Joshi YB, Chu J, Pratico D. The 12-15-lipoxygenase is a modulator of Alzheimer's-related tau pathology in vivo. *Aging Cell*. 2013;12(6):1082–90. https://doi.org/10.1111/acel.12136.
64. Do TM, Alata W, Dodacki A, Traversy MT, Chacun H, Pradier L, et al. Altered cerebral vascular volumes and solute transport at the blood-brain barriers of two transgenic mouse models of Alzheimer's disease. *Neuropharmacology*. 2014;81:311–7.
65. Neff RA, Wang M, Vatansever S, Guo L, Ming C, Wang Q, et al. Molecular subtyping of Alzheimer's disease using RNA sequencing data reveals novel mechanisms and targets. *Sci Adv*. 2021;7(2). https://doi.org/10.1126/sciadv.abb5398.
66. Hu YS, Xin J, Hu Y, Zhang L, Wang J. Analyzing the genes related to Alzheimer's disease via a network and pathway-based approach. *Alzheimers Res Ther*. 2017;9:29.
67. Jonsson T, Stefansson H, Steinberg S, Jonsdottir I, Jonsson PV, Snaedal J, et al. Variant of TREM2 associated with the risk of Alzheimer's disease. *N Engl J Med*. 2013;368(2):107–16. https://doi.org/10.1056/NEJMoa1211103.
68. Chen Y, Fang L, Chen S, Zhou H, Fan Y, Lin L, et al. Gut microbiome alterations precede cerebral amyloidosis and microglial pathology in a mouse model of Alzheimer's disease. *Biomed Res Int*. 2020;2020:8456596–15. https://doi.org/10.1155/2020/8456596.
69. Perez-Nievas BG, Serrano-Pozo A. Deciphering the astrocyte reaction in Alzheimer's disease. *Front Aging Neurosci*. 2018;10:114. https://doi.org/10.3389/fnagi.2018.00114.
70. Liddelow SA, Barres BA. Reactive astrocytes: production, function, and therapeutic potential. *Immunity*. 2017;46(6):957–67. https://doi.org/10.1016/j.immuni.2017.06.006.
71. Song WM, Colonna M. The identity and function of microglia in neurodegeneration. *Nat Immunol*. 2018;19(10):1048–58. https://doi.org/10.1038/s41590-018-0212-1.
72. Colom-Cadena M, Spires-Jones T, Zetterberg H, Blennow K, Caggiano A, DeKosky ST, et al. The clinical promise of biomarkers of synapse damage or loss in Alzheimer's disease. *Alzheimers Res Ther*. 2020;12(1):21. https://doi.org/10.1186/s13195-020-00588-4.
73. Del Campo M, Hoozemans JJ, Dekkers LL, Rozemuller AJ, Korth C, Muller-Schiffmann A, et al. BRI2-BRICHOS is increased in human amyloid plaques in early stages of Alzheimer's disease. *Neurobiol Aging*. 2014;35(7):1596–604. https://doi.org/10.1016/j.neurobiolaging.2014.01.007.
74. Dolfe L, Tambaro S, Tigro H, Del Campo M, Hoozemans JJM, Wiehager B, et al. The Bri2 and Bri3 BRICHOS domains interact differently with Abeta42 and Alzheimer amyloid plaques. *J Alzheimers Dis Rep*. 2018;2(1):27–39. https://doi.org/10.3233/ADR-170051.
75. Soler-Lopez M, Zanzoni A, Lluis R, Stelzl U, Aloy P. Interactome mapping suggests new mechanistic details underlying Alzheimer's disease. *Genome Res*. 2011;21(3):364–76. https://doi.org/10.1101/gr.114280.110.
76. Diamond MS, Farzan M. The broad-spectrum antiviral functions of IFIT and IFITM proteins. *Nat Rev Immunol*. 2013;13(1):46–57. https://doi.org/10.1038/nri3344.
77. Nalls MA, Plagnol V, Hernandez DG, Sharma M, Sheerin UM, Saad M, et al. Imputation of sequence variants for identification of genetic risks for Parkinson's disease: a meta-analysis of genome-wide association studies. *Lancet*. 2011;377:641–9.
78. Huynh DP, Scoles DR, Nguyen D, Pulst SM. The autosomal recessive juvenile Parkinson disease gene product, parkin, interacts with and ubiquitinates synaptotagmin XI. *Hum Mol Genet*. 2003;12(20):2587–97. https://doi.org/10.1093/hmg/ddg269.
79. Wang C, Kang X, Zhou L, Chai Z, Wu Q, Huang R, et al. Synaptotagmin-11 is a critical mediator of parkin-linked neurotoxicity and Parkinson's disease-like pathology. *Nat Commun*. 2018;9(1):81. https://doi.org/10.1038/s41467-017-02593-y.
80. Shimojo M, Madara J, Pankow S, Liu X, Yates J 3rd, Sudhof TC, et al. Synaptotagmin-11 mediates a vesicle trafficking pathway that is essential for development and synaptic plasticity. *Genes Dev*. 2019;33(5-6):365–76. https://doi.org/10.1101/gad.320077.118.
81. Bai B, Wang X, Li Y, Chen PC, Yu K, Dey KK, et al. Deep multilayer brain proteomics identifies molecular networks in Alzheimer's disease progression. *Neuron*. 2020;105(6):975–991.e7. https://doi.org/10.1016/j.neuron.2019.12.015.
82. Lamb J, Crawford ED, Peck D, Modell JW, Blat IC, Wrobel MJ, et al. The Connectivity Map: using gene-expression signatures to connect small molecules, genes, and disease. *Science*. 2006;313(5795):1929–35. https://doi.org/10.1126/science.1132939.
83. Heneka MT, Carson MJ, El Khoury J, Landreth GE, Brosseron F, Feinstein DL, et al. Neuroinflammation in Alzheimer's disease. *Lancet Neurol*. 2015;14(4):388–405. https://doi.org/10.1016/S1474-4422(15)70016-5.
84. Daniels MJ, Rivers-Auty J, Schilling T, Spencer NG, Watremez W, Fasolino V, et al. Fenamate NSAIDs inhibit the NLRP3 inflammasome and protect against Alzheimer's disease in rodent models. *Nat Commun*. 2016;7(1):12504. https://doi.org/10.1038/ncomms12504.
85. Woodling NS, Colas D, Wang Q, Minhas P, Panchal M, Liang X, et al. Cyclooxygenase inhibition targets neurons to prevent early behavioural decline in Alzheimer's disease model mice. *Brain*. 2016;139(7):2063–81. https://doi.org/10.1093/brain/aww117.
86. in t' Veld BA, Ruitenberg A, Hofman A, Launer LJ, van Duijn CM, Stijnen T, Breteler MM, Stricker BH: Nonsteroidal antiinflammatory drugs and the risk of Alzheimer's disease. *N Engl J Med* 2001, 345:1515-1521, Nonsteroidal Antiinflammatory Drugs and the Risk of Alzheimer's Disease, 21, doi: https://doi.org/10.1056/NEJMoa010178.
87. Vlad SC, Miller DR, Kowall NW, Felson DT. Protective effects of NSAIDs on the development of Alzheimer disease. *Neurology*. 2008;70:1672–7.
88. Mostafavi S, Gaiteri C, Sullivan SE, White CC, Tasaki S, Xu J, et al. A molecular network of the aging human brain provides insights into the pathology and cognitive decline of Alzheimer disease. *Nat Neurosci*. 2018;21(6):811–9. https://doi.org/10.1038/s41593-018-0154-9.

89. Schorn C, Frey B, Lauber K, Janko C, Strysio M, Keppeler H, et al. Sodium overload and water influx activate the NALP3 inflammasome. *J Biol Chem*. 2011;286(1):35–41. https://doi.org/10.1074/jbc.M110.139048.
90. Encinas M, Iglesias M, Liu Y, Wang H, Muhaisen A, Cena V, et al. Sequential treatment of SH-SY5Y cells with retinoic acid and brain-derived neurotrophic factor gives rise to fully differentiated, neurotrophic factor-dependent, human neuron-like cells. *J Neurochem*. 2000;75(3):991–1003. https://doi.org/10.1046/j.1471-4159.2000.0750991.x.
91. Podlisny MB, Ostaszewski BL, Squazzo SL, Koo EH, Rydell RE, Teplow DB, et al. Aggregation of secreted amyloid beta-protein into sodium dodecyl sulfate-stable oligomers in cell culture. *J Biol Chem*. 1995;270(16):9564–70. https://doi.org/10.1074/jbc.270.16.9564.
92. Janssens GE, Meinema AC, Gonzalez J, Wolters JC, Schmidt A, Guryev V, et al. Protein biogenesis machinery is a driver of replicative aging in yeast. *Elife*. 2015;4:e08527. https://doi.org/10.7554/eLife.08527.
93. Wei YN, Hu HY, Xie GC, Fu N, Ning ZB, Zeng R, et al. Transcript and protein expression decoupling reveals RNA binding proteins and miRNAs as potential modulators of human aging. *Genome Biol*. 2015;16(1):41. https://doi.org/10.1186/s13059-015-0608-2.
94. de Sousa AR, Penalva LO, Marcotte EM, Vogel C. Global signatures of protein and mRNA expression levels. *Mol Biosyst*. 2009;5:1512–26. https://doi.org/10.1039/b908315d.
95. Greenbaum D, Colangelo C, Williams K, Gerstein M. Comparing protein abundance and mRNA expression levels on a genomic scale. *Genome Biol*. 2003;4(9):117. https://doi.org/10.1186/gb-2003-4-9-117.
96. Maier T, Guell M, Serrano L. Correlation of mRNA and protein in complex biological samples. *FEBS Lett*. 2009;in t'(24):3966–73. https://doi.org/10.1016/j.febslet.2009.10.036.
97. Drummond E, Nayak S, Faustin A, Pires G, Hickman RA, Askenazi M, et al. Proteomic differences in amyloid plaques in rapidly progressive and sporadic Alzheimer's disease. *Acta Neuropathol*. 2017;133(6):933–54. https://doi.org/10.1007/s00401-017-1691-0.
98. Weggen S, Eriksen JL, Das P, Sagi SA, Wang R, Pietrzik CU, et al. A subset of NSAIDs lower amyloidogenic Abeta42 independently of cyclooxygenase activity. *Nature*. 2001;414(6860):212–6. https://doi.org/10.1038/35102591.
99. Nissen SE, Yeomans ND, Solomon DH, Luscher TF, Libby P, Husni ME, et al. Cardiovascular safety of celecoxib, naproxen, or ibuprofen for arthritis. *N Engl J Med*. 2016;375:2519–29.
100. Hershey LA, Lipton RB. Naproxen for presymptomatic Alzheimer disease: is this the end, or shall we try again. *Neurology*. 2019;92(18):829–30. https://doi.org/10.1212/WNL.0000000000007233.
101. Heneka MT, Golenbock DT, Latz E. Innate immunity in Alzheimer's disease. *Nat Immunol*. 2015;16(3):229–36. https://doi.org/10.1038/ni.3102.
102. Ardura-Fabregat A, Boddeke E, Boza-Serrano A, Brioschi S, Castro-Gomez S, Ceyzeriat K, et al. Targeting neuroinflammation to treat Alzheimer's disease. *CNS Drugs*. 2017;31(12):1057–82. https://doi.org/10.1007/s40263-017-0483-3.
103. Munafo A, Burgaletto C, Di Benedetto G, Di Mauro M, Di Mauro R, Bernardini R, et al. Repositioning of immunomodulators: a ray of hope for Alzheimer's disease. *Front Neurosci*. 2020;14:614643. https://doi.org/10.3389/fnins.2020.614643.
104. Qiu C, Winblad B, Fratiglioni L. The age-dependent relation of blood pressure to cognitive function and dementia. *Lancet Neurol*. 2005;4(8):487–99. https://doi.org/10.1016/S1474-4422(05)70141-1.
105. Andrieu S, Coley N, Lovestone S, Aisen PS, Vellas B. Prevention of sporadic Alzheimer's disease: lessons learned from clinical trials and future directions. *Lancet Neurol*. 2015;14(9):926–44. https://doi.org/10.1016/S1474-4422(15)00153-2.
106. Katsouri L, Vizcaychipi MP, McArthur S, Harrison I, Suarez-Calvet M, Lleo A, et al. Prazosin, an alpha(1)-adrenoceptor antagonist, prevents memory deterioration in the APP23 transgenic mouse model of Alzheimer's disease. *Neurobiol Aging*. 2013;34(4):1105–15. https://doi.org/10.1016/j.neurobiolaging.2012.09.010.
107. Wang J, Ono K, Dickstein DL, Arrieta-Cruz I, Zhao W, Qian X, et al. Carvedilol as a potential novel agent for the treatment of Alzheimer's disease. *Neurobiol Aging*. 2011;32(2321):e2321–12.
108. Koren G, Norton G, Radinsky K, Shalev V. Chronic use of beta-blockers and the risk of Parkinson's disease. *Clin Drug Investig*. 2019;39(5):463–8. https://doi.org/10.1007/s40261-019-00771-y.
109. Hopfner F, Hoglinger GU, Kuhlenbaumer G, Pottegard A, Wod M, Christensen K, et al. Beta-adrenoreceptors and the risk of Parkinson's disease. *Lancet Neurol*. 2020;19(3):247–54. https://doi.org/10.1016/S1474-4422(19)30400-4.
110. Fornasiero EF, Mandad S, Wildhagen H, Alevra M, Rammner B, Keihani S, et al. Precisely measured protein lifetimes in the mouse brain reveal differences across tissues and subcellular fractions. *Nat Commun*. 2018;9(1):4230. https://doi.org/10.1038/s41467-018-06519-0.

Publisher's Note